Laurin Hauser, BSc

Numerical simulation of cone penetration tests using G-PFEM

MASTERARBEIT

zur Erlangung des akademischen Grades

Diplom-Ingenieur

Masterstudium Bauingenieurwissenschaften – Geotechnik und Wasserbau

eingereicht an der

Technischen Universität Graz

Betreuer

Ao.Univ.-Prof. Dipl.-Ing. Dr.techn. M.Sc. tit.Univ.-Prof.
Helmut F. Schweiger

Institut für Bodenmechanik und Grundbau
Computational Geotechnics Group

Graz, Mai 2017

Eidesstattliche Erklärung

Ich erkläre an Eides statt, dass ich die vorliegende Arbeit selbstständig verfasst, andere als die angegebenen Quellen/Hilfsmittel nicht benutzt, und die den benutzten Quellen wörtlich und inhaltlich entnommenen Stellen als solche kenntlich gemacht habe.

Graz, am ……………………… ……………………………………………….

(Unterschrift)

Statutory declaration

I declare that I have authored this thesis independently, that I have not used other than the declared sources / resources, and that I have explicitly marked all material which has been quoted either literally or by content from the used sources.

Graz, ………………………… ……………………………………………….

(signature)

Preface of the author

Undoubtedly, many people have supported me throughout my higher studies. I would like to take this opportunity to thank them for their contributions.

First and foremost, I would like to thank Ao.Univ.-Prof. Dipl.-Ing. Dr.techn. Helmut F. Schweiger for suggesting the topic and thereby introducing me to an interesting field of research. I greatly appreciate his mentoring and continuous advice. Certainly, the work on the thesis would not have been possible without the collaboration and support of Prof. Marcos Arroyo and Lluís Monforte from the Polytechnic University of Catalonia.

I would like to thank all my friends and colleagues for their advice and friendship which made the years in Graz a special time. I very much enjoyed working and developing my thesis alongside the other graduands at the Institute of Soil Mechanics and Foundation Engineering.

Finally, let me express a special thanks to my family. I greatly appreciate the moral and linguistic support of my sister Anna Chiara and I am very grateful for the continuous encouragement of my parents Tiziana and Walter during my studies.

Kurzfassung

Die numerische Simulation von Drucksondierungen (CPT) ist eine herausfordernde Fragestellung im Gebiet der Geotechnik. Die auftretenden großen Verschiebungen und Dehnungen erfordern zum einen ein entsprechendes physikalisches Modell und zum anderen ein geeignetes numerisches Lösungsverfahren. Forscher an der Polytechnischen Universität von Katalonien (UPC) und am International Center for Numerical Methods in Engineering (CIMNE) in Barcelona entwickelten den Particle Finite Element Method (PFEM) code G-PFEM, wodurch die numerische Simulation von Eindringvorgängen in voll gesättigten porösen Medien ermöglicht wird.

Die Grundgleichungen werden mit Hilfe eines Updated Lagrangian Ansatzes formuliert. Die PFEM basiert auf wiederholter Neuvernetzung der kritischen Bereiche des Integrationsgebiets. Dem entstehenden, rechnerischen Mehraufwand wird durch Verwendung linearer Elemente entgegengewirkt. Letztere neigen zu volumetrischem Locking, wodurch eine stabilisierte, gemischte Formulierung des Problems erforderlich wird.

Im Zuge der Arbeit wurden Nachrechnungen von in-situ Sondierungen durchgeführt, um den Einfluss von unterschiedlichen Randbedingungen, wie der Durchlässigkeit des Bodens oder der Eindringgeschwindigkeit der Sonde, auf den gemessenen Spitzendruck, die Mantelreibung und den Wasserdruck bei teildrainierten Verhältnissen zu untersuchen. Die Vergleichbarkeit der Ergebnisse ist gegeben. In Bezugnahme auf durchgeführte Modellversuche wurde das Verformungsverhalten von Schluffen bei Drucksondierungen analysiert, wobei die beobachteten lokalen Drainagevorgänge im Zuge der Simulation noch nicht im Detail nachgebildet werden konnten.

Abstract

The numerical simulation of cone penetration tests (CPT) is a challenging field in geotechnics. Both the underlying physical model and the numerical method need to be capable of taking into account large deformations and displacements within the problem domain. Researchers at the Polytechnic University of Catalonia (UPC) and the International Center for Numerical Methods in Engineering (CIMNE) have developed a Particle Finite Element Method (PFEM) code named G-PFEM which conducts fully coupled analysis of penetration problems in saturated porous media.

An updated Lagrangian description is used in order to formulate the governing equations. The PFEM is based on frequent remeshing of critical regions of the problem domain adding additional computational cost to the solving process. Therefore, the use of linear elements in combination with a stabilized mixed formulation of the governing equations helps to reduce the computational effort and at the same time cope with the phenomenon of volumetric locking associated with linear elements.

Recalculations of available CPTs were performed allowing the examination of the influence of changing boundary conditions, such as permeability of the soil or penetration velocity of the cone, on the measured tip resistance, sleeve friction and pore water pressure. It was found that the recalculation with G-PFEM provides comparable results for partially drained conditions. Furthermore, small scale experiments on the soil deformation of silts during CPTs were studied by numerical means whereby the resulting local drainage behaviour could not yet be reproduced in detail within the simulation.

Table of contents

1 Introduction 1

2 Cone Penetration Tests 2

3 Theoretical background on G-PFEM 4

3.1 Basics of Continuum Mechanics 4

3.2 Particle Finite Element Method 7

3.3 Boundary value problem 9

3.3.1 Linear Momentum 10

3.3.2 Mass Balance 10

3.3.3 Governing equations 12

3.4 Stabilized mixed formulation 12

3.5 Finite Element discretization in G-PFEM 14

3.6 Contact modelling 15

3.7 Constitutive relation 16

4 Anisotropic permeability in G-PFEM 18

4.1 Consolidation of an elastic finite soil layer 18

4.2 Summary 20

5 Numerical simulation of CPTu 21

5.1 Determination of hydraulic conductivity from CPTu 21

5.1.1 ‘On-the-fly’ method 21

5.1.2 Numerical calculations 23

5.1.3 Summary 27

5.2 Recalculation of in-situ CPTu 28

5.2.1 Calculation 1: CPTu with rough and smooth cone 28

5.2.2 Calculation set 2: Impact of varying penetration velocity 31

5.2.3 Calculation set 3: Partially drained conditions during CPT 33

5.2.4 Summary 36

5.3 Behaviour of silts during CPTu 37

5.3.1 Deformation behaviour around the cone 37

5.3.2 Stress paths analysis 42

5.3.3 Summary 45

6 Conclusion & Outlook 47

7 Bibliography 48

List of figures

Fig. 1 CPTu cone with piezometer positions (Lunne et al. 1997). 2

Fig. 2 Mapping of material vector $d\boldsymbol{X}$ from initial/reference to current configuration (Coussy 2004). 5

Fig. 3 Basic steps of PFEM going from a cloud of nodes (C) over the definition of a volume (V) to the generation of a mesh (M) (Oñate et al. 2011). 9

Fig. 4 Model of axisymmetric elastic soil layer on rigid, rough and impermeable base. 18

Fig. 5 Comparison of normalized displacement at centre point ($\mathrm{r} = \mathrm{z} = 0$) versus time factor T for different permeability ratios $\gamma 2$ (Chen 2004). 19

Fig. 6 Comparison of normalized pore pressure pq versus dimensionless depth zH along the symmetry axis at given instances of time T (Chen 2004). 20

Fig. 7 Proposed bi-linear $KD - Bq\,Qt$ relationship with modified data points from Elsworth & Lee (2007) taken from Chai et al. (2011). 23

Fig. 8 Axisymmetric model of the domain. 24

Fig. 9 Computed excess pore pressure $\Delta u2$ versus normalized depth for varying penetration velocities, both isotropic and anisotropic permeabilities and changing initial stress conditions. 25

Fig. 10 Double logarithmic plot of resulting $\Delta \mathrm{u2}$ in terms of KD and BqQt for the cases (a) to (c) at depths of 1, 5 and 10 m. 27

Fig. 11 Calculation 1 – rough cone: Contour plots of nodal Jacobian Θ [-] (a) and the water pressure pw [kPa] (b) at a penetration depth of around 22 cm. 29

Fig. 12 Calculation 1: CPTu log of recalculated in-situ test with smooth and rough cone. 30

Fig. 13 Calculation set 2: CPTu log for varying penetration velocities with rough cone. 31

Fig. 14 Calculation set 2: Contour plots of the magnitude of Darcy flow [m/s] for penetration velocities of 1 cm/s (a), 2 cm/s (b) and 3 cm/s (c) at a penetration depth of 22 cm. 32

Fig. 15 Calculation set 3: CPTu log for varying penetration velocities with smooth cone. 34

Fig. 16 Calculation set 3: Contour plots of nodal Jacobian Θ [-] for penetration velocities of 1 cm/s (a), 2 cm/s (b) and 3 cm/s (c) at a penetration depth of 22 cm. 34

Fig. 17 Calculation set 3: Contour plots of water pressure pw [kPa] for penetration velocities of 1 cm/s (a), 2 cm/s (b) and 3 cm/s (c) at a penetration depth of 22 cm. 35

Fig. 18 Calculation set 3: Contour plots of the magnitude of Darcy flow [m/s] for penetration velocities of 1 cm/s (a), 2 cm/s (b) and 3 cm/s (c) at a penetration depth of 22 cm. 36
Fig. 19 Incremental volumetric strain $\Delta\epsilon vol$ (a) and shear strain $\Delta\epsilon shear$ (b) around the cone between 56 and 61 mm of penetration (Paniagua et al. 2013). 37
Fig. 20 Incremental volumetric strain $\Delta\epsilon vol$ and shear strain $\Delta\epsilon shear$ for the penetration increments 56 to 61 mm (a) & (d), 156 to 161 mm (b) & (e) and 256 to 261 mm (c) & (f) for calculation set 3 (isotropic, reduced permeability and v_c = 2 cm/s); volume increase is positive. 39
Fig. 21 Contour plots of pore pressure distribution pw [kPa] around the cone after 56 mm (a), 156 mm (b) and 256 mm (c) of penetration. 40
Fig. 22 Contour plots of incremental Jacobian $\Delta\Theta$ (a) and incremental plastic shear strain (b) after 156 mm of penetration; $\Delta\Theta > 1$ equals volume expansion. 41
Fig. 23 Contour plots of nodal Jacobian Θ [-] around the cone after 56 mm (a), 156 mm (b) and 256 mm (c) of penetration; $\Theta > 1$ equals volume expansion........ 42
Fig. 24 Stress path for point P01 (0, -0.2): elastic unloading and loading (0 – A); undrained loading until CS (A – B); stress redistribution at CS and unloading before cone arrives at stress point (B – C). 43
Fig. 25 Stress path for point P02 (0, -0.3): elastic unloading and loading (0 – A); undrained loading until CS (A – B); stress redistribution at CS with jump of stress point before cone arrives at stress point (B – C). 44
Fig. 26 Stress invariants P [kPa] (a) and $J2$ [kPa] (b) at the penetration depth of 0.28 m. 44
Fig. 27 Stress path for point P19 (0.02, -0.2): undrained loading until CS (0 – A); stress redistribution at CS (A – B); stress oscillation as cone shoulder passes by (B – C); elastic unloading (C – D); elasto-plastic unloading causing dilation (D – E). 46

List of tables

Tab. 1 Input parameters for elastic soil layer in consolidation example. 19
Tab. 2 MCC input parameters for silty sand. 24
Tab. 3 Mean excess pore pressure $\Delta u2$ and resulting 'on-the-fly' hydraulic conductivity k_{otf} at different depths. 26
Tab. 4 Input parameters for clayey to silty soil layer averaged over 5 m thick layer. ...28
Tab. 5 Calculation 1: MCC input parameters for clayey/silty soil layer. 29
Tab. 6 Calculation 1: Comparison of calculated and measured values for qc, fs and $u2$. 30
Tab. 7 Calculation set 2: Results of calculated values (qc, fs, $u2$) for varying penetration velocities. 32
Tab. 8 Calculation set 3: MCC input parameters for clayey to silty layer. 33
Tab. 9 Comparison of calculated mean values of qc and $u2$ of calculation sets 2 and 3 for varying penetration velocities. 33

List of symbols and abbreviations

Capital letters

A_c	[cm²]	base area of cone
A_s	[cm²]	area of friction sleeve
B_q	[-]	dimensionless water pressure ratio
C_c	[-]	compression index
C_s	[-]	swelling index
${}^{n}C, {}^{n+1}C$		particle cloud at time steps n and $n+1$
$\boldsymbol{C}$		Right Cauchy-Green strain tensor
E	[kPa]	Young's modulus
E_s	[kPa]	constrained modulus
$\boldsymbol{E}$		Green-Lagrange strain tensor
$\delta\,{}^{t+\Delta t}_{t}\boldsymbol{E}$		virtual Green-Lagrange strain tensor referring config. $t+\Delta t$ to t
${}^{1}_{0}\boldsymbol{E}$		Green-Lagrange strain tensor referring config. 1 to 0 (initial)
${}^{2}_{0}\boldsymbol{E}$		Green-Lagrange strain tensor referring config. 2 to 0 (initial)
${}^{\Delta}_{0}\boldsymbol{E}$		incremental Green-Lagrange strain tensor referring to config. 0
$\boldsymbol{F}$		deformation gradient
$\boldsymbol{F}_d$		deviatoric part of the deformation gradient
$\boldsymbol{F}_v$		volumetric part of the deformation gradient
$\boldsymbol{F}^e$		elastic part of the deformation gradient
$\boldsymbol{F}^p$		plastic part of the deformation gradient
$\breve{\boldsymbol{F}}$		assumed deformation gradient
$\breve{\boldsymbol{F}}^e$		elastic part of the assumed deformation gradient
$\breve{\boldsymbol{F}}^p$		plastic part of the assumed deformation gradient
${}^{1}_{0}\boldsymbol{F}$		deformation gradient referring configuration 0 (initial) to 1
${}^{2}_{0}\boldsymbol{F}$		deformation gradient referring configuration 0 (initial) to 2
${}^{2}_{1}\boldsymbol{F}$		deformation gradient referring configuration 1 to 2
G	[kPa]	shear modulus
G_0	[kPa]	constant part of the shear modulus in hyperelastic model
$\boldsymbol{G}_{(n)}$		general strain tensor in Lagrangian description
G		space of admissible virtual Jacobians
H	[m]	thickness of soil layer
$\boldsymbol{H}$		Hencky strain tensor in Lagrangian description
$\boldsymbol{I}$		unit matrix
I_r	[-]	rigidity index

J		Jacobian (determinant of deformation gradient)
J^e		elastic Jacobian
${}_0^1J$		Jacobian from configuration 0 to 1
${}_0^2J$		Jacobian from configuration 0 to 2
${}_1^2J$		Jacobian from configuration 1 to 2
J_2		second stress invariant
K_D	[-]	dimensionless hydraulic conductivity
K_w	[kPa]	water bulk modulus
K_0	[-]	earth pressure coefficient at rest
$\boldsymbol{K}$		stiffness matrix
$\boldsymbol{K}^{pen}$		stiffness matrix in constraining system
$\boldsymbol{K}_{p0}$	[$\mathrm{m^2kPa^{-1}s^{-1}}$]	permeability tensor at initial reference configuration
M	[-]	slope of critical state line
M	[kPa]	constrained modulus
${}^{n}M, {}^{n+1}M$		mesh at time steps n and $n+1$
$\boldsymbol{N}$		global shape function vector
$\boldsymbol{N}_u$		global shape function matrix for approximation of $\boldsymbol{u}$
Q		space of admissible virtual pore pressures
Q_t	[-]	dimensionless tip resistance
R	[m]	base radius of the cone
$\boldsymbol{R}$		orthogonal rotation-tensor
$\boldsymbol{S}$		second Piola-Kirchhoff stress tensor (PK2)
${}^{t+\Delta t}_{\;\;t}\boldsymbol{S}$		PK2 at $t+\Delta t$ referring to configuration t
T	[-]	dimensionless time factor
U, U_1, U_2	[$\mathrm{ms^{-1}}$]	penetration velocity
$\boldsymbol{U}(\boldsymbol{X}, t)$	[m]	displacement vector
$\boldsymbol{U}$		symmetric stretching-tensor in Lagrangian description
V		space of admissible virtual displacements
V_1, V_2		volume at configuration 1 and 2
$\Delta\dot{V}$	[$\mathrm{m^3s^{-1}}$]	displaced volume per time during penetration
${}^{n}V, {}^{n+1}V$		volume at time steps n and $n+1$
${}^{t}V, {}^{t+\Delta t}V$		volume of the domain at time t and $t+\Delta t$
$\boldsymbol{V}$		symmetric stretching-tensor in Eulerian description
dV		volume element in reference configuration
${}^{t+\Delta t}W$		virtual work at time $t+\Delta t$
$\boldsymbol{X}$		position of material particle in reference configuration

$d\boldsymbol{X}$		line element in reference configuration

Small letters

a	[m]	radius of circular load
$\boldsymbol{a}_{(n)}$		general strain tensor in Eulerian description
b	[m]	model width
$\boldsymbol{b}$		Left Cauchy-Green strain tensor
$\boldsymbol{b}^e$		elastic part of the Left Cauchy-Green strain tensor
$\underline{\boldsymbol{b}}$		body force
c_h	[$\mathrm{m^2yr^{-1}}$]	horizontal coefficient of consolidation
e_0	[-]	initial void ratio
$\boldsymbol{e}$		Euler-Almansi strain tensor
$f(\boldsymbol{\tau}')$		yield surface as a function of effective Kirchhoff stresses
f_s	[kPa]	measured sleeve friction
$\boldsymbol{f}$		load vector
$\boldsymbol{f}^{pen}$		load vector in constraining system
$\bar{g}$	[$\mathrm{m^3s^{-1}}$]	imposed boundary flow
$\boldsymbol{g}$	[$\mathrm{ms^{-2}}$]	gravity
h, h_1, h_2	[m]	model heights
$\boldsymbol{h}$		Hencky strain tensor in Eulerian description
$\boldsymbol{h}^e$		elastic part of Hencky strain tensor in Eulerian description
$\boldsymbol{h}_d^e$		elastic, deviatoric part of Hencky strain tensor in E.D.
$\boldsymbol{h}_v^e$		elastic, volumetric part of Hencky strain tensor in E.D.
$\boldsymbol{h}_f$		contact force on fluid phase
$\boldsymbol{h}_s$		contact force on solid phase
i_R	[-]	hydraulic gradient at cavity
k	[$\mathrm{ms^{-1}}$]	hydraulic conductivity
k_{otf}	[$\mathrm{ms^{-1}}$]	‘on-the-fly’ estimate of the hydraulic conductivity
k_v	[$\mathrm{ms^{-1}}$]	hydraulic conductivity in vertical direction
$\boldsymbol{k}_p$	[$\mathrm{m^2kPa^{-1}s^{-1}}$]	permeability tensor in current configuration
$k_{p,h}$	[$\mathrm{m^2kPa^{-1}s^{-1}}$]	horizontal permeability
$k_{p,iso}$	[$\mathrm{m^2kPa^{-1}s^{-1}}$]	isotropic permeability
$k_{p,v}$	[$\mathrm{m^2kPa^{-1}s^{-1}}$]	vertical permeability
n	[-]	porosity
$\boldsymbol{n}$		outward normal vector
p	[Pa]	water pressure

p_c	[kPa]	isotropic preconsolidation pressure
p_{c0}	[kPa]	isotropic reference preconsolidation pressure
p_w	[kPa]	pore water pressure
$p_{w,top}$	[kPa]	pore water pressure on top of the domain
p_w^h		piecewise linear approximation of pore water pressure
$\tilde{\boldsymbol{p}}_{\boldsymbol{w}}$		discrete nodal pore water pressure vector
p_{w0}	[kPa]	initial pore water pressure
$\bar{p}_w$	[kPa]	imposed boundary pore pressure
p_0	[kPa]	reference pressure
q		virtual pore pressure
q	[Pa]	axisymmetric load
q_{flow}	[m^{3}s^{-1}]	half-spherical water flow
q_c	[kPa]	measured tip resistance
q_t	[kPa]	corrected tip resistance
s_u	[kPa]	undrained shear strength
t	[s]	time
Δt	[s]	time increment
$\bar{\boldsymbol{t}}$		imposed boundary traction
u_0	[kPa]	initial water pressure
u_1	[kPa]	water pressure at tip position of the cone
u_2	[kPa]	water pressure at shoulder position of the cone
u_3	[kPa]	water pressure above friction sleeve
u_m	[kPa]	total, undrained pore pressure
Δu_R	[kPa]	excess pore water pressure at cavity
Δu_2	[kPa]	excess water pressure at shoulder position of the cone
$\Delta \bar{u}_2$	[kPa]	mean excess water pressure at shoulder position of the cone
$\boldsymbol{u}^h$		piecewise linear approximation of displacement
$\tilde{\boldsymbol{u}}$		discrete nodal displacement vector
$\boldsymbol{u}_0$	[m]	initial displacement vector
$\bar{\boldsymbol{u}}$	[m]	imposed boundary displacement
dv	[m^3]	volume element in current configuration
v_c	[ms^{-1}]	penetration velocity of the cone
v_R	[ms^{-1}]	water flow velocity at the cavity
$\boldsymbol{v}_d$	[ms^{-1}]	Darcian velocity vector
$\boldsymbol{v}_f$	[ms^{-1}]	velocity vector of fluid phase
$\boldsymbol{v}_s$	[ms^{-1}]	velocity vector of solid phase

w	[-]	penalty factor
$w(r,z,T)$	[m]	surface subsidence
x_0, x_1, x_2		line element in configuration 0, 1 or 2
$\boldsymbol{x}$	[m]	position of material particle in current configuration
$d\boldsymbol{x}$	[m]	line element in current configuration

Greek letters

α	[-]	coupling term between volumetric and deviatoric behaviour
α, β	[-]	empirical correction factor
α_c	[°]	cone tip angle
α_n	[-]	net area ratio
α_s^{Θ}	[-]	stabilization parameter for the nodal Jacobian
Γ_g		flow sub-boundary
Γ_{p_w}		pore pressure sub-boundary
$\Gamma_{\bar{t}}$		traction sub-boundary
Γ_u		displacement sub-boundary
γ	[kNm^{-3}]	specific weight
γ_s	[kNm^{-3}]	specific weight of the soil
γ_w	[kNm^{-3}]	specific weight of the water
γ^2	[-]	permeability ratio
$\Delta\epsilon_{vol}$	[-]	incremental volumetric strain
$\Delta\epsilon_{shear}$	[-]	incremental shear strain
$\Delta\epsilon_1, \Delta\epsilon_2, \Delta\epsilon_3$		incremental principle strains
$\delta^{t+\Delta t}\boldsymbol{\epsilon}$		virtual strain tensor at time $t + \Delta t$
$\bar{\boldsymbol{\epsilon}}$		small strain tensor
$\boldsymbol{\epsilon}_d^e$		elastic, deviatoric Hencky strain tensor
ϵ_v^e		elastic, volumetric Hencky strain
ζ		virtual nodal Jacobian
$\boldsymbol{\eta}$		virtual displacement
Θ	[-]	nodal approximation of the Jacobian
$\Delta\Theta$	[-]	incremental nodal approximation of the Jacobian
Θ^h		piecewise linear approximation of nodal Jacobian
$\widetilde{\boldsymbol{\Theta}}$		discrete nodal Jacobian vector
Θ_L		Lode's angle
κ	[-]	swelling index
κ^*	[-]	modified swelling index

Λ	[-]	plastic volumetric strain ratio
λ	[-]	compression index
λ^*	[-]	modified compression index
ν	[-]	Poisson’s ratio
μ	[kPa]	shear modulus
π'		mean pressure of Kirchhoff stress tensor
ρ	[tm^{-3}]	overall density
ρ_f, ρ_w	[tm^{-3}]	density of fluid/water constituent
ρ_s	[tm^{-3}]	density of solid constituent
σ_{v0}	[kPa]	total, vertical in-situ stress
σ'_{v0}	[kPa]	effective, vertical in-situ stress
$\sigma_{v,top}$	[kPa]	total, vertical stress on top of the domain
$\sigma'_{v,top}$	[kPa]	effective, vertical stress on top of the domain
$\boldsymbol{\sigma}$		Cauchy stress tensor
${}^{t+\Delta t}\boldsymbol{\sigma}$		Cauchy stress tensor at time $t + \Delta t$
$\boldsymbol{\sigma}_f$		partial fluid Cauchy stress tensor
$\boldsymbol{\sigma}_s$		partial solid Cauchy stress tensor
$\boldsymbol{\sigma}'$		effective Cauchy stress tensor
$\breve{\boldsymbol{\sigma}}$		assumed Cauchy stress tensor
τ		stabilization parameter for the pore water pressure
$\boldsymbol{\tau}'$		effective Kirchhoff stress tensor
$\boldsymbol{\tau}_d$		deviatoric part of the effective Kirchhoff stress tensor
ϕ'	[°]	effective friction angle
$\phi_{contact}$	[°]	contact friction angle between soil and cone
$\boldsymbol{\phi}(\boldsymbol{X}, t)$		mapping from reference to current configuration
$\boldsymbol{\phi}^{-1}(\boldsymbol{x}, t)$		mapping from current to reference configuration
Ψ		stored energy function
ψ	[°]	dilation angle
Ω_t		domain at current configuration

Abbreviations

CPT	Cone Penetration Test
CS	Critical State
E.D.	Eulerian/Spatial description
FEM	Finite Element Method
FPL	fluid pressure Laplacian method
L.D.	Lagrangian/Material description
MCC	Modified Cam Clay
OCR [-]	over consolidation ratio
PFEM	Particle Finite Element Method
PPP	polynomial pressure projection

1 Introduction

The determination of soil properties is a central and challenging task in geotechnical engineering. Laboratory tests offer a wide range of investigation methods whereby removal, transport and installation of the soil sample can easily disturb the specimen and influence the test results. Therefore, in-situ testing becomes more and more important. Cone penetrations testing (CPT) represents one of those methods where a metal cone is pushed into the soil at a constant penetration rate while measuring the tip resistance and sleeve friction. Additional measurement of the pore water pressure can be included in a CPTu. The measured quantities allow determining the local stratigraphy, the ground water conditions and mechanical soil properties, indirectly via correlations. Thereby, the quality of the derived parameters depends strongly on the applicability of the available correlations. Reasonable results are provided for both the application under predominantly drained or undrained conditions whereas the behaviour under partial drainage is still a major issue in ongoing research. Numerical simulations of this kind of penetration problems can play an important role in investigating the partially drained behaviour of certain soils during CPT and, as a future goal, contribute to the validation and improvement of the proposed correlations. Moreover, such silty soils can be found in alpine basins in Austria and consequently its characterization is of substantial relevance.

The present work involves numerical studies on CPTu based on a Particle Finite Element Method (PFEM) aiming to gain a better understanding of the coupled soil-water interaction during the penetration process. Initially, a brief overview on cone penetration testing is given before presenting the theoretical framework of the numerical method as well as an extension of the application in terms of considering anisotropic permeability. Eventually, numerical studies on the estimation of the hydraulic conductivity, a recalculation of an in-situ CPTu and investigations on the deformation behaviour of silts are presented.

2 Cone Penetration Tests

Cone penetration testing is an in-situ soil investigation method where a metal cone is pushed into the soil at a constant penetration velocity. The cone is equipped with load cells enabling to measure the tip resistance $\mathrm{q_c}$ and the sleeve friction $\mathrm{f_s}$. Furthermore, the conduction of a CPTu includes the measurement of pore water pressures at the $\mathrm{u_1}$, $\mathrm{u_2}$ and $\mathrm{u_3}$ positions through additional piezometers at the cone (see Fig. 1).

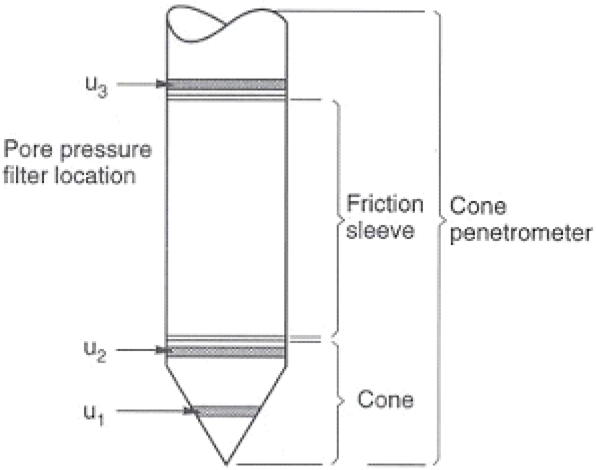

Fig. 1 CPTu cone with piezometer positions (Lunne et al. 1997).

Usually, the cone measures 10 cm² of base area ($\mathrm{A_c}$) which corresponds to a diameter of 3.57 cm. For some applications, the cone area can vary between 5 and 15 cm². The friction sleeve has a standard area of 150 cm² ($\mathrm{A_s}$) while the aperture angle α_c at the cone tip equals 60°. The standard penetration velocity is 2 cm/s. Furthermore, the corrected tip resistance $\mathrm{q_t}$ results after subtracting a portion of the pore pressure at the shoulder position according to the net area ratio a_n:

$$q_t = q_c + (1 - a_n)\, u_2 \qquad (1)$$

Empirical correlations allow the determination of soil parameters based on the measured quantities (Lunne et al. 1997):

- Initial state parameter: γ, ψ, $\mathrm{K_0}$, OCR
- Strength parameters: $\mathrm{s_u}$, ϕ'
- Deformation characteristics: E, G, M
- Flow characteristics: k, $\mathrm{c_h}$

The interested reader is referred to Sachsenhofer (2012) for more information on the interpretation of CPTu measurements.

However, the soil resistance and pore pressure during penetration are strongly dependent on the drainage conditions. Most of the proposed correlations are derived for either drained (sand) or undrained conditions (clay) making the interpretation for partially drained silts difficult (Lunne et al. 1997).

3 Theoretical background on G-PFEM

The conduction of a cone penetration test causes large deformations and displacements of the penetrated soil. Thus, its simulation is a challenging field in numerical geotechnics since small strain theory does not provide reasonable results. In order to deal with this problem both the underlying physical model and the numerical method need to be capable of treating large deformations and displacements within the problem domain.

Researchers at the Polytechnic University of Catalonia (UPC) and the International Center for Numerical Methods in Engineering (CIMNE) have developed a Particle Finite Element Method (PFEM) code named G-PFEM which enables fully coupled analysis of penetration problems in saturated porous media (Monforte et al. 2016, Monforte et al. 2017). The application is implemented in the FEM framework Kratos (Dadvand et al. 2010).

3.1 Basics of Continuum Mechanics

At first, some kinematic definitions are introduced based on Kelly (2012). Let $\boldsymbol{X}$ be the position of a material particle in an initial (or reference) configuration and $\boldsymbol{x}$ be its position in the current configuration after the body has undergone deformation (see Fig. 2). The change of position is described as a mapping between the two configurations

$$\boldsymbol{x} = \boldsymbol{\phi}(\boldsymbol{X}, t) \tag{2}$$

$$\boldsymbol{X} = \boldsymbol{\phi}^{-1}(\boldsymbol{x}, t) \tag{3}$$

where Eq. (2) represents the ***Material*** or ***Lagrangian*** description (L.D.) and Eq. (3) stands for the ***Spatial*** or ***Eulerian*** description (E.D.). Furthermore, Fig. 2 shows the transformation of a line element $\mathrm{d}\mathbf{X}$ from the reference to the current configuration giving $\mathrm{d}\mathbf{x} = \mathbf{F}\,\mathrm{d}\mathbf{X}$, with:

$$\boldsymbol{F} = Grad\,\boldsymbol{\phi} = \frac{d\boldsymbol{x}}{d\boldsymbol{X}} \tag{4}$$

The deformation gradient $\mathbf{F}$ is a fundamental measure in continuum mechanics characterizing the stretching and rotation during the deformation of a body. It is therefore useful to decompose the deformation gradient into an orthogonal rotation-tensor $\mathbf{R}$ and the symmetric stretching-tensors $\mathbf{U}$ or $\mathbf{V}$ yielding $\mathbf{F} = \mathbf{R}\,\mathbf{U}$ (L.D.) or rather $\mathbf{F} = \mathbf{V}\,\mathbf{R}$ (E.D.). Rigid body translation has no impact on the deformation gradient. In analogy to the mapping $\boldsymbol{\phi}$ and $\boldsymbol{\phi}^{-1}$, the inverse $\mathbf{F}^{-1}$ must exist.

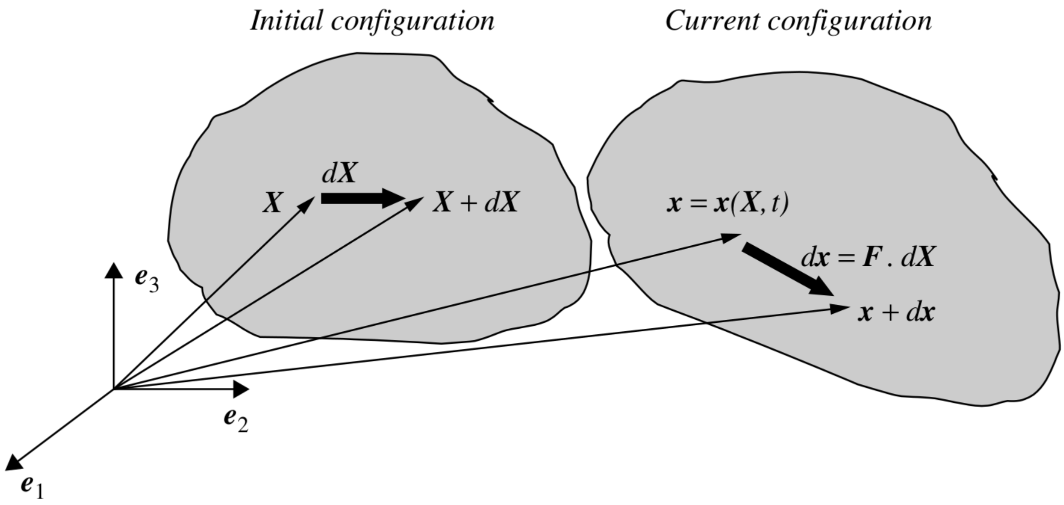

Fig. 2 Mapping of material vector $d\boldsymbol{X}$ from initial/reference to current configuration (Coussy 2004).

Additionally, the determinant J of the deformation gradient is introduced describing the volume change between the reference (dV) and the current configuration (dv):

$$J = \det(\boldsymbol{F})$$

$$dv = J\, dV \tag{5}$$

Since $\mathbf{F}^{-1}$ exists and negative volumes do not make physical sense, $\mathrm{J} > 0$ is required. No volume change gives a value of $\mathrm{J} = 1$. The deformation gradient $\mathbf{F}$ can also be multiplicatively decomposed into a volumetric $\mathbf{F}_\mathrm{v}$ and deviatoric part $\mathbf{F}_\mathrm{d}$ whereby the condition $\det(\mathbf{F}_\mathrm{d}) = 1$ must hold. This results in:

$$\boldsymbol{F} = \boldsymbol{F}_v\, \boldsymbol{F}_d$$

$$\boldsymbol{F}_v = J^{1/3}\, \boldsymbol{I} \tag{6}$$

$$\boldsymbol{F}_d = J^{-1/3}\, \boldsymbol{F}$$

With regard to the formulation of a constitutive relation between stress and strain, the Green-Lagrange strain tensor $\mathbf{E}$ is introduced as

$$\boldsymbol{E} = \tfrac{1}{2}(\boldsymbol{F}^T\boldsymbol{F} - \boldsymbol{I}) = \tfrac{1}{2}(\boldsymbol{C} - \boldsymbol{I}) \tag{7}$$

with $\mathbf{C}$ being the Right Cauchy-Green strain tensor. According to Bathe (2014), $\mathbf{C}$ is rewritten in terms of the rotation and stretching tensors $\mathbf{R}$ and $\mathbf{U}$ giving:

$$\boldsymbol{C} = (\boldsymbol{U}^T\ \boldsymbol{R}^T)\ (\boldsymbol{R}\ \boldsymbol{U}) = \boldsymbol{U}^2 \tag{8}$$

Thus, the Green-Lagrange strain tensor depends only on the stretching tensor $\mathbf{U}$ and is invariant under rigid body rotation and translation. Note that $\mathbf{E}$ can be expressed in terms of the displacement $\mathbf{U}(\mathbf{X}, \mathrm{t}) = \mathbf{x}(\mathbf{X}, \mathrm{t}) - \mathbf{X}$ and contains the engineering small strain tensor $\bar{\boldsymbol{\epsilon}}_{\mathrm{ij}}$ and the quadratic term $\frac{1}{2}(\frac{\partial \mathrm{U_k}}{\partial \mathrm{X_i}} \frac{\partial \mathrm{U_k}}{\partial \mathrm{X_j}})$:

$$\begin{gathered} \boldsymbol{E}_{ij} = \frac{1}{2}\left(\frac{\partial U_i}{\partial X_j} + \frac{\partial U_j}{\partial X_i} + \frac{\partial U_k}{\partial X_i}\frac{\partial U_k}{\partial X_j}\right) \\ \bar{\boldsymbol{\epsilon}}_{ij} = \frac{1}{2}\left(\frac{\partial U_i}{\partial X_j} + \frac{\partial U_j}{\partial X_i}\right) \end{gathered} \tag{9}$$

However, the Green-Lagrange strain tensor is not the only strain measure. A more general form of the strain tensor both in Lagrangian (L.D.) and Eulerian (E.D.) description is given by (Altenbach 2015)

$$\begin{aligned} \boldsymbol{G}_{(n)} &= \tfrac{1}{2n}(\boldsymbol{U}^{2n} - \boldsymbol{I}) = \tfrac{1}{2n}(\boldsymbol{C}^{n} - \boldsymbol{I}) && \text{(L.D.)} \\ \boldsymbol{a}_{(n)} &= \tfrac{1}{2n}(\boldsymbol{I} - \boldsymbol{V}^{-2n}) = \tfrac{1}{2n}(\boldsymbol{I} - \boldsymbol{b}^{-n}) && \text{(E.D.)} \end{aligned} \tag{10}$$

with the Left Cauchy-Green strain tensor $\mathbf{b} = \mathbf{V}^2 = \mathbf{F}\ \mathbf{F}^{\mathrm{T}}$.

Setting $\mathrm{n} = 1$ the tensors $\mathbf{G}$ and $\mathbf{a}$ result in the Green-Lagrange and Euler-Almansi strain tensors. Besides that, the case where $\mathrm{n} = 0$ is of interest as it gives the logarithmic ***Hencky*** strain tensor $\mathbf{H}$ or rather $\mathbf{h}$:

$$\begin{aligned} \boldsymbol{G}_{(n=0)} &= \ln \boldsymbol{U} = \tfrac{1}{2}\ln \boldsymbol{C} \overset{\mathrm{def}}{=} \boldsymbol{H} && \text{(L.D.)} \\ \boldsymbol{a}_{(n=0)} &= \ln \boldsymbol{V} = \tfrac{1}{2}\ln \boldsymbol{b} \overset{\mathrm{def}}{=} \boldsymbol{h} && \text{(E.D.)} \end{aligned} \tag{11}$$

This strain measure allows an additive decomposition of the tensor into a deviatoric and volumetric part, as for the small strain tensor $\bar{\boldsymbol{\epsilon}}$.

3.2 Particle Finite Element Method

An ***Updated Lagrangian formulation*** for the continuum equations is used where the last known configuration at time t serves as reference and thus changes with every time step Δt while the current configuration at time $t + \Delta t$ is the unknown one.

The basic idea is pointed out by considering the principle of virtual work at time $t + \Delta t$ where the internal work equals the external one for every admissible virtual displacement (Bathe 2014):

$$\int_{^{t+\Delta t}V} {}^{t+\Delta t}\boldsymbol{\sigma}\, \delta\, {}^{t+\Delta t}\boldsymbol{\epsilon}\; d\,{}^{t+\Delta t}V = {}^{t+\Delta t}W \tag{12}$$

Thereby, the internal work results as the integral of the Cauchy stress tensor ${}^{t+\Delta t}\boldsymbol{\sigma}$ times the virtual strain tensor $\delta\,{}^{t+\Delta t}\boldsymbol{\epsilon}$ over the unknown volume ${}^{t+\Delta t}V$. With the current volume not being known Eq. (12) is rewritten in terms of a known reference configuration. Therefore, a new stress measure is introduced, in the form of the second Piola-Kirchhoff stress tensor:

$$\boldsymbol{S} = \mathrm{J}\, \boldsymbol{F}^{-1}\, \boldsymbol{\sigma}\, \boldsymbol{F}^{-T} \tag{13}$$

The virtual strain tensor is expressed as a virtual Green-Lagrange strain tensor and the integration can now be carried out on the known domain ${}^{t}V$ of the reference configuration at time t in order to solve for the unknown internal forces:

$$\int_{^{t}V} {}^{t+\Delta t}_{t}\boldsymbol{S}\, \delta\, {}^{t+\Delta t}_{t}\boldsymbol{E}\; d\,{}^{t}V = {}^{t+\Delta t}W \tag{14}$$

In a next step the focus lies on an effective numerical method for solving problems where large deformations and displacements of the domain are involved.

The ***Particle Finite Element Method*** is based on a ***Particle Method*** meaning that the problem domain is represented by a sum of material particles carrying all the information. The position of the particles and so also the domain changes during the computation. In order to calculate the updated solution at time $t + \Delta t$ the particles at reference state t are treated as nodes and a FEM solves the governing equations. Required integration points are redefined with each remeshing step. The procedure is illustrated in Fig. 3 describing the steps according to Oñate et al. (2011) for a coupled problem including a solid and a fluid domain:

- The starting point is a cloud of particles ${}^{n}C$ at the last known reference configuration at time n. Each particle can be identified as either a fluid, solid or boundary node and carries its state variables, such as displacements and pressures.
- A crucial step is now defining the domain boundaries and so going from a cloud of points to a volume ${}^{n}V$. Note that parts of the domain(s) can also be separated or re-united. Techniques like the ***α-shape method*** are used for identifying the domain boundaries. The interested reader is therefore referred to Oñate et al. (2011).
- Based on the defined volume a mesh ${}^{n}M$ is built, with the particles serving as nodes, in order to initiate the FEM solution procedure. At this point new nodes can be inserted or old ones removed depending on the local nodal density. In this way the quality of the mesh is corrected by avoiding on the one hand the generation of large elements in regions where the nodes moved far apart and on the other hand the generation of small elements in regions where the nodes are concentrated. The triangular meshing is based on a ***Delaunay*** tessellation (see Oñate et al. (2011) and Monforte et al. (2016)) which maximizes the angles of each element and so reduces element distortion.
- New nodes and integration points inherit variables from the last known configuration whereby different interpolation methods can be applied. However, now the actual solving process using the FEM is carried out in order to solve the governing equations for the next updated configuration at time $t + 1$. Consequently, one obtains a new particle cloud ${}^{n+1}C$ with an updated position of the particles and updated state variables.
- The process starts again until the desired final time step is reached.

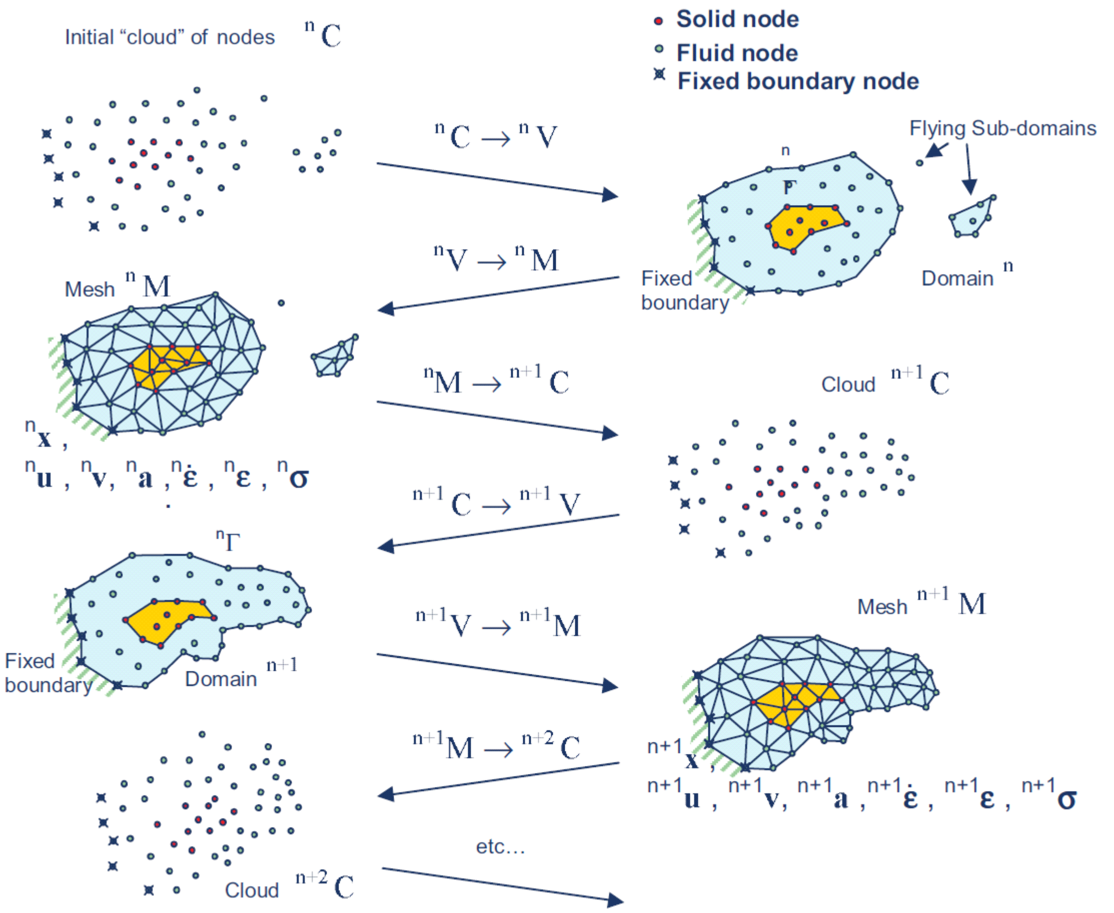
Initial "cloud" of nodes ${}^{n}C$
● Solid node
○ Fluid node
✕ Fixed boundary node
${}^{n}C \rightarrow {}^{n}V$
Flying Sub-domains
${}^{n}\Gamma$
Fixed boundary
Domain ^{n}
${}^{n}V \rightarrow {}^{n}M$
Mesh ${}^{n}M$
${}^{n}\mathbf{x}$,
${}^{n}\mathbf{u}$, ${}^{n}\mathbf{v}$, ${}^{n}\mathbf{a}$, ${}^{n}\dot{\boldsymbol{\varepsilon}}$, ${}^{n}\boldsymbol{\varepsilon}$, ${}^{n}\boldsymbol{\sigma}$
${}^{n}M \rightarrow {}^{n+1}C$
Cloud ${}^{n+1}C$
${}^{n+1}C \rightarrow {}^{n+1}V$
${}^{n}\Gamma$
Fixed boundary
Domain ${}^{n+1}$
${}^{n+1}V \rightarrow {}^{n+1}M$
Mesh ${}^{n+1}M$
${}^{n+1}\mathbf{x}$,
${}^{n+1}\mathbf{u}$, ${}^{n+1}\mathbf{v}$, ${}^{n+1}\mathbf{a}$, ${}^{n+1}\dot{\boldsymbol{\varepsilon}}$, ${}^{n+1}\boldsymbol{\varepsilon}$, ${}^{n+1}\boldsymbol{\sigma}$
${}^{n+1}M \rightarrow {}^{n+2}C$
Cloud ${}^{n+2}C$
etc…

Fig. 3 Basic steps of PFEM going from a cloud of nodes (C) over the definition of a volume (V) to the generation of a mesh (M) (Oñate et al. 2011).

The continuous remeshing of the domain leads to an increased computational effort. Counteractively, the use of low order elements, linear triangles in 2D and linear tetrahedrons in 3D, helps to reduce the computation costs but at the same time opens the door for locking phenomena in the FEM solution. Especially for applications in soil mechanics where nearly incompressible behaviour of the soil occurs, volumetric locking of linear elements is a frequent issue. In G-PFEM this is addressed by introducing a mixed, stabilized formulation of the underlying boundary value problem in order to keep the advantage of using linear elements.

3.3 Boundary value problem

According to the theory of ***Poromechanics*** the governing equations are formulated for a fully saturated porous media. The interested reader is referred to Larsson & Larsson (2002), Borja & Alarcón (1995) and Sun et al. (2013) for further reading.

3.3.1 Linear Momentum

We consider a unit volume composed of a solid and fluid phase in the current configuration. The overall density is $\rho = (1-n)\rho_s + n\,\rho_f$ with n being the porosity and ρ_s and ρ_f being the densities of the solid and fluid components, respectively. Thus, the quasi static equation for linear momentum is formulated in terms of partial stresses $\boldsymbol{\sigma}_s$ and $\boldsymbol{\sigma}_f$ for each phase separately according to Larsson & Larsson (2002):

$$\begin{aligned} \nabla \cdot \boldsymbol{\sigma}_s + \rho_s(1-n)\boldsymbol{g} + \boldsymbol{h}_s &= \mathbf{0} \\ \nabla \cdot \boldsymbol{\sigma}_f + \rho_f n\,\boldsymbol{g} + \boldsymbol{h}_f &= \mathbf{0} \\ \boldsymbol{h}_s + \boldsymbol{h}_f &= \mathbf{0} \end{aligned} \tag{15}$$

Thereby, the expressions $\mathbf{h}_s$ and $\mathbf{h}_f$ represent the contact forces between the two phases which cancel out in order to obtain equilibrium. Hence, the equations are combined giving the more general expression

$$\nabla \cdot \boldsymbol{\sigma} + \underline{\boldsymbol{b}} = \mathbf{0} \tag{16}$$

with the total Cauchy stress tensor $\boldsymbol{\sigma} = \boldsymbol{\sigma}_s + \boldsymbol{\sigma}_f$ and the body force vector $\underline{\mathbf{b}} = \rho\,\mathbf{g}$.

In a next step, the effective stress principle is introduced. Therefore, the partial fluid stress tensor is rewritten as

$$\boldsymbol{\sigma}_f = n\,p_w\mathbf{I} \tag{17}$$

where p_w stands for the water pressure per unit volume. Consequently, the total stress tensor is decomposed into effective stresses of the soil skeleton and pore water pressure yielding:

$$\begin{aligned} \boldsymbol{\sigma} &= \boldsymbol{\sigma}' + p_w\mathbf{I} \\ \boldsymbol{\sigma}' &= \boldsymbol{\sigma}_s + (1-\tfrac{1}{n})\boldsymbol{\sigma}_f \end{aligned} \tag{18}$$

3.3.2 Mass Balance

Again, we consider a unit volume of mixture and formulate the Lagrangian mass balance (Borja & Alarcón 1995) for both components giving

$$\frac{d}{dt}\left(\rho_f n\right) + \nabla \cdot \left(\rho_f n \boldsymbol{v}_f\right) = 0$$
$$\frac{d}{dt}\left(\rho_s(1-n)\right) + \nabla \cdot \left(\rho_s(1-n)\boldsymbol{v}_s\right) = 0 \tag{19}$$

with the respective velocity vectors $\mathbf{v}_\mathrm{s}$ and $\mathbf{v}_\mathrm{f}$ of the two phases. At this point, the relative Darcian velocity $\mathbf{v}_\mathrm{d} = \mathrm{n}(\mathbf{v}_\mathrm{f} - \mathbf{v}_\mathrm{s})$ is introduced and the equations are rewritten:

$$n\frac{d}{dt}\left(\rho_f\right) + \rho_f \frac{d}{dt}(n) + \nabla \cdot \left(\rho_f(\boldsymbol{v}_d + n\boldsymbol{v}_s)\right) = 0$$
$$(1-n)\frac{d}{dt}(\rho_s) - \rho_s \frac{d}{dt}(n) + \nabla \cdot \left(\rho_s(\boldsymbol{v}_s - n\boldsymbol{v}_s)\right) = 0 \tag{20}$$

Now, the solid phase is assumed incompressible causing ρ_s to be independent of time and space. Furthermore, the spatial variation of ρ_f is neglected. Eventually, dividing the equations by the respective phase densities ρ_f or rather ρ_s and adding them up gives:

$$\frac{n}{\rho_f}\dot{\rho}_f + \nabla \cdot \boldsymbol{v}_d + \nabla \cdot \boldsymbol{v}_s = 0 \tag{21}$$

Referring to Sun et al. (2013), the fluid phase is assumed to have a linear elastic relation between the logarithmic volumetric strains and the pore pressure. Hence, the expression for the change of fluid density in time from Eq. (21) can be rewritten in terms of the water bulk modulus K_w and the time derivative of p_w:

$$\frac{n}{\rho_f}\dot{\rho}_f = -\frac{1}{\mathrm{K}_w}\dot{p}_w \tag{22}$$

The flow of the pore fluid is described by Darcy's law where $\mathbf{v}_\mathrm{d}$ depends on the permeability of the porous medium $\mathbf{k}_\mathrm{p}$ times the hydraulic gradient:

$$\boldsymbol{v}_d = -\boldsymbol{k}_p\left(\nabla p_w + \rho_w \boldsymbol{g}\right) \tag{23}$$

Since $(\nabla \mathrm{p}_\mathrm{w} + \rho_\mathrm{w}\mathbf{g})$ has the unit Pa/m, $\mathbf{k}_\mathrm{p}$ must be given in terms of m²/(Pa*s) so that $\mathbf{v}_\mathrm{d}$ results in m/s. Furthermore, Larsson & Larsson (2002) discuss that $\mathbf{k}_\mathrm{p}$ should be seen as a macroscopic quantity which depends on the soil deformation. The authors remark that $\mathbf{k}_\mathrm{p}$ in the current configuration relates to $\mathbf{K}_\mathrm{p0}$ in the initial reference configuration via:

$$\boldsymbol{k}_p = J^{-1}\boldsymbol{F}\,\boldsymbol{K}_{p0}\,\boldsymbol{F}^t \tag{24}$$

In this way, the rotation of the principle axes is taken into account which is especially important for the case of anisotropic permeability.

3.3.3 Governing equations

Finally, the governing equations according to Monforte et al. (2016) are given as:

$$\begin{aligned} &\nabla \cdot \boldsymbol{\sigma} + \underline{\boldsymbol{b}} = \mathbf{0} && in\ \Omega_t \\ &-\frac{1}{\mathrm{K}_w}\dot{p}_w + \nabla \cdot \boldsymbol{v}_s + \nabla \cdot \boldsymbol{v}_d = 0 && in\ \Omega_t \end{aligned} \qquad (25)$$

The following initial and boundary conditions hold

$$\begin{aligned} &\boldsymbol{u}(\boldsymbol{X}, t = 0) = \boldsymbol{u}_0 && in\ \Omega_0 \\ &p_w(\boldsymbol{X}, t = 0) = p_{w0} && in\ \Omega_0 \\ &\boldsymbol{u}(\boldsymbol{X}, t) = \bar{\boldsymbol{u}} && in\ \Gamma_u \\ &\boldsymbol{\sigma} \cdot \boldsymbol{n} = \bar{\boldsymbol{t}} && in\ \Gamma_{\bar{t}} \\ &p_w(\boldsymbol{X}, t) = \bar{p}_w && in\ \Gamma_{p_w} \\ &-\boldsymbol{n} \cdot \boldsymbol{v}_d = \bar{g} && in\ \Gamma_g \end{aligned} \qquad (26)$$

where the domain's boundary $\partial\Omega$ is divided into the sub-boundaries Γ_u, $\Gamma_{\bar{\mathrm{t}}}$, $\Gamma_{\mathrm{p_w}}$ and Γ_g with the respective imposed displacement $\bar{\mathbf{u}}$, traction $\bar{\mathbf{t}}$, water pressure $\bar{\mathrm{p}}_\mathrm{w}$ and flow $\bar{\mathrm{g}}$.

3.4 Stabilized mixed formulation

Having in mind that the chosen FE space of piecewise linear shape functions will cause locking effects in the solution, a stabilized mixed formulation of the governing equations is introduced. The derived boundary value problem (section 3.3.3) is typically solved in terms of the displacement vector $\mathbf{u}(\mathbf{X}, \mathrm{t})$ and the pore pressure $\mathrm{p_w}(\mathbf{X}, \mathbf{t})$. Monforte et al. (2016) presented and tested mixed formulations of the boundary value problem where additional degrees of freedom and corresponding constraining equations are introduced. For the present work, the focus lies on the mixed ***displacement-Jacobian-water pressure*** ($\mathbf{u}$ - J - $\mathrm{p_w}$) formulation (Monforte et al. 2016) with the Jacobian being the additional degree of freedom. Hence, Eq. (25) is extended to

$$\begin{aligned} &\nabla \cdot \breve{\boldsymbol{\sigma}} + \underline{\boldsymbol{b}} = \mathbf{0} && in\ \Omega_t \\ &J - \Theta = 0 && in\ \Omega_t \\ &-\frac{1}{\mathrm{K}_w}\dot{p}_w + \nabla \cdot \boldsymbol{v}_s + \nabla \cdot \boldsymbol{v}_d = 0 && in\ \Omega_t \end{aligned} \tag{27}$$

where Θ stands for the nodal approximation of the volume change which must be equal to $\mathrm{J} = \det(\mathbf{F})$ within the whole domain. According to the decomposition from Eq. (6), the assumed deformation gradient

$$\breve{\boldsymbol{F}} = (\Theta^{1/3}\,\boldsymbol{I})\,(J^{-1/3}\,\boldsymbol{F}) \tag{28}$$

can be formulated whereby the volumetric part is expressed by the additional degree of freedom Θ. Hence, the divergence of the Cauchy stress tensor is now applied on an assumed stress tensor $\breve{\boldsymbol{\sigma}}$ depending on $\breve{\mathbf{F}}$.

The equation set is then written in its weak form by pre-multiplication of a weighting function and integration over the (current) domain Ω_t and boundary Γ yielding

$$\int_{\Omega_t} \nabla\boldsymbol{\eta} : \breve{\boldsymbol{\sigma}}\, d\Omega_t = \int_{\Omega_t} \boldsymbol{\eta} \cdot \underline{\boldsymbol{b}}\, d\Omega_t + \int_{\Gamma_{\bar{t}}} \boldsymbol{\eta} \cdot \bar{\boldsymbol{t}}\, d\Gamma \tag{29}$$

$$\int_{\Omega_t} \zeta(J - \Theta)\, \frac{1}{J}\, d\Omega_t = 0 \tag{30}$$

$$\int_{\Omega_t} q\nabla \cdot \boldsymbol{v}_s\, \frac{1}{J}\, d\Omega_t + \int_{\Omega_t} \nabla q \cdot \boldsymbol{v}_d\, \frac{1}{J}\, d\Omega_t - \int_{\Omega_t} q\, \frac{1}{K_w}\, \dot{p}_w\, \frac{1}{J}\, d\Omega_t = \int_{\Gamma_{\bar{g}}} q\, \bar{g}\, d\Gamma \tag{31}$$

where $\eta \in \mathrm{V}$, $\zeta \in \mathrm{G}$ and $\mathrm{q} \in \mathrm{Q}$ are the virtual displacements, virtual nodal Jacobians and virtual pressures given in the respective spaces V, G and Q. The stabilization of the problem is achieved by adding stabilizing terms to the weak formulation, more specifically to Eq. (30) and (31). The basic principles are pointed out according to Monforte et al. (2016). The interested reader is referred to the latter source for further information.

Firstly, the ***polynomial pressure projection*** (PPP) method is used adding the term

$$\int_{\Omega_t} (\zeta - \breve{\zeta}) \frac{\alpha_s^{\Theta}}{\mu} (\Theta - \breve{\Theta}) \, d\Omega_t = 0 \tag{32}$$

to Eq. (30) with μ being the shear modulus of the material and α_s^{Θ} the stabilization parameter of the Jacobian. Note that α_s^{Θ} is an input value.

Secondly, the mass balance Eq. (31) is stabilized with the ***fluid pressure Laplacian*** (FPL) method where the expression

$$\int_{\Omega_t} \tau \, \nabla q \cdot \boldsymbol{k}_p \cdot \nabla \dot{p}_w \frac{1}{J} \, d\Omega_t = 0 \tag{33}$$

is added to the weak form. The parameter τ depends on the element size, the bulk modulus and permeability tensor of the material and the time step (Preisig & Prévost 2011). Additionally, τ is scaled by a user defined stabilization factor for the water pressure within G-PFEM.

3.5 Finite Element discretization in G-PFEM

Monforte et al. (2016) use linear, triangular elements in 2D. Consequently, the field variables $\mathbf{u}$, Θ and $\mathrm{p_w}$ can be approximated as

$$\begin{aligned} \boldsymbol{u}^h &= \boldsymbol{N_u} \, \widetilde{\boldsymbol{u}} \\ \Theta^h &= \boldsymbol{N} \, \widetilde{\boldsymbol{\Theta}} \\ \mathrm{p}_\mathrm{w}^h &= \boldsymbol{N} \, \widetilde{\mathbf{p}}_{\boldsymbol{w}} \end{aligned} \tag{34}$$

with the linear global shape function vector $\mathbf{N} = [\mathrm{N}_1, \mathrm{N}_2, \dots, \mathrm{N}_\mathrm{n}]$ and discrete nodal values vectors $\widetilde{\mathbf{u}}$, $\widetilde{\boldsymbol{\Theta}}$ and $\widetilde{\mathbf{p}}_\mathbf{w}$. Since $\mathbf{u}$ is a vectorial quantity the matrix $\mathbf{N_u} = [\mathrm{N}_1\mathbf{I}, \mathrm{N}_2\mathbf{I}, \dots, \mathrm{N}_\mathrm{n}\mathbf{I}]$ is introduced. The discrete, weak, stabilized formulation of the governing equations is extensively discussed in Monforte et al. (2016).

So far, the problem has been formulated in the current configuration (using an Eulerian description). In order to integrate over a known domain, the quantities are transformed to the updated reference configuration at the last known time t. Generally, tensors and vectors can be transformed between Eulerian and Lagrangian description using push-forward or pull-back operations. Considering the Euler-Almansi $\mathbf{e}$ and Green-Lagrange $\mathbf{E}$ strain tensors the two operations yield:

$$\boldsymbol{e} = \boldsymbol{F}^{-T}\,\boldsymbol{E}\,\boldsymbol{F}^{-1} \qquad \text{(push-forward)}$$
$$\boldsymbol{E} = \boldsymbol{F}^{T}\,\boldsymbol{e}\,\boldsymbol{F} \qquad \text{(pull-back)} \tag{35}$$

Note that the operations are not unique and depend on covariant/contravariant components of the vector or tensor (Kelly 2012).

The equations are solved using an implicit integration scheme in time. Therefore, the time derivative of the water pressure and the soil velocity vector are replaced by a forward finite difference formulation (Monforte et al. 2016, Monforte et al. 2017).

3.6 Contact modelling

The contact modelling between the deformable soil-water body and the penetrating, rigid cone is a central aspect in G-PFEM. With each time step a certain incremental displacement is imposed on the boundary nodes, corresponding to a Dirichlet boundary condition. More generally speaking, a constraint is applied to the system through the ***penalty method***.

The basic idea is explained according to Felippa (2004): For a linear system $\mathbf{K}\,\mathbf{u} = \mathbf{f}$, the arbitrary constraint $\mathrm{u}_1 + 2\,\mathrm{u}_2 = 1$ is assumed and rewritten as:

$$\begin{bmatrix} 1 & 2 & 0 & \cdots & 0 \end{bmatrix} \begin{bmatrix} u_1 \\ \vdots \\ u_n \end{bmatrix} = 1 \tag{36}$$

Then, the equation is pre-multiplied by the transposed coefficient vector and a scaling factor w, also known as the penalty factor, giving:

$$w \begin{bmatrix} 1 \\ 2 \\ 0 \\ \vdots \\ 0 \end{bmatrix} \begin{bmatrix} 1 & 2 & 0 & \cdots & 0 \end{bmatrix} \begin{bmatrix} u_1 \\ \vdots \\ u_n \end{bmatrix} = w \begin{bmatrix} 1 \\ 2 \\ 0 \\ \vdots \\ 0 \end{bmatrix}$$
$$\boldsymbol{K}^{pen}\boldsymbol{u} = \boldsymbol{f}^{pen} \tag{37}$$

Finally, Eq. (37) is added to the original system. This results in a new linear system which incorporates the imposed constraining equation but depends on w:

$$(\boldsymbol{K} + \boldsymbol{K}^{pen})\ \boldsymbol{u} = \boldsymbol{f} + \boldsymbol{f}^{pen} \tag{38}$$

Felippa (2004) compares the application of a constraint to adding a rigid or rather very stiff element to the system. Rigidity requires $w \rightarrow \infty$ and leads to an exact incorporation of the constraint but at the same time produces an ill-conditioned system of equations. Thus, it is evident that the penalty method is an approximate way to treat constraints, where a balance between accurate incorporation (increase of w) and solvability (decrease of w) needs to be found. However, the implementation is straightforward.

3.7 Constitutive relation

In order to model elasto-plastic behaviour for large strains it is common practice to decompose the deformation gradient into an elastic and plastic part giving $\mathbf{F} = \mathbf{F}^{\mathrm{e}}\ \mathbf{F}^{\mathrm{p}}$ or rather $\check{\mathbf{F}} = \check{\mathbf{F}}^{\mathrm{e}}\ \check{\mathbf{F}}^{\mathrm{p}}$ for the assumed deformation gradient. The soil is described by a ***Modified Cam Clay*** (MCC) model whereby the hyperelastic model by Houlsby is considered for the elastic regime (Monforte et al. 2016).

In hyperelasticity a stored energy function Ψ must exist. Its partial derivative with respect to a strain measure results in the corresponding energy conjugate stress measure. Eq. (39) shows an example for the second Piola-Kirchhoff stress tensor and the Green-Lagrange stain tensor. In this way, kinematic and force variables are connected giving a constitutive relation (Kelly 2012).

$$\boldsymbol{S} = \frac{\partial \Psi(\boldsymbol{E}^{e})}{\partial \boldsymbol{E}^{e}} \tag{39}$$

The adopted strain measure is the Hencky strain tensor $\mathbf{h}$ in E.D. with its elastic part $\mathbf{h}^{\mathrm{e}} = \ln(\mathbf{b}^{\mathrm{e}})/2$. The latter is further decomposed into its volumetric and deviatoric parts $\mathbf{h}_{\mathrm{v}}^{\mathrm{e}}$ and $\mathbf{h}_{\mathrm{d}}^{\mathrm{e}}$ which allows to formulate:

$$\begin{aligned} \epsilon_v^e &= \boldsymbol{I} :\ \boldsymbol{h}^e = \ln(J^e) \\ \boldsymbol{\epsilon}_d^e &= \boldsymbol{h}_d^e = \tfrac{1}{2}\ln(J^{e\ -2/3}\boldsymbol{b}^e) \end{aligned} \tag{40}$$

Thus, the stress-strain relation follows in terms of effective Kirchhoff stress $\boldsymbol{\tau}' = \mathrm{J}\boldsymbol{\sigma}'$ according to Monforte et al. (2016):

$$\boldsymbol{\tau}' = \pi'\boldsymbol{I} + \boldsymbol{\tau}_d$$

$$\pi' = -p_0 \exp\left(\frac{-\epsilon_v^e}{\kappa^*}\right)\left(1 + \frac{\alpha}{\kappa^*} \parallel \boldsymbol{\epsilon}_d^e \parallel^2\right) \tag{41}$$

$$\boldsymbol{\tau}_d = 2\left(G_0 + \alpha\, p_0 \exp\left(\frac{-\epsilon_v^e}{\kappa^*}\right)\right)\boldsymbol{\epsilon}_d^e$$

Thereby, p_0 is a reference pressure, G_0 stands for the constant part of the shear modulus and $\kappa^* = \frac{\kappa}{1+\mathrm{e}_0}$ is the modified swelling index which results from the swelling index κ and the initial void ratio e_0. The parameter $\alpha \geq 0$ defines the coupling between volumetric and deviatoric material behaviour. A value equal to zero means no coupling.

Eventually, the plastic behaviour can be described by means of a yield surface

$$f(\boldsymbol{\tau}') = \left(\frac{\sqrt{3}\,J_2}{M(\theta_\mathrm{L})}\right)^2 + \pi'(\pi' - p_c) \tag{42}$$

formulated in terms of stress invariants of the Kirchhoff stress $(\pi', \mathrm{J}_2, \theta_\mathrm{L})$ and the appropriate hardening law

$$p_c = p_{c0} \exp\left(\frac{-\epsilon_v^p}{\lambda^* - \kappa^*}\right) \tag{43}$$

with the isotropic preconsolidation pressure $\mathrm{p_c}$ or rather its refence value $\mathrm{p_{c0}}$, the slope of the critical state line M as a function of the Lode's Angle θ_L and the modified compression index $\lambda^* = \frac{\lambda}{1+e_0}$. An associated flow rule is adopted (Monforte et al. 2016).

4 Anisotropic permeability in G-PFEM

Natural soil deposits are often characterized by highly anisotropic hydraulic permeabilities. The resulting effect on the water flow, and consequently on the system behaviour, is crucial. Therefore, this feature has been included in G-PFEM allowing the definition of an anisotropic permeability tensor $\mathbf{k}_\mathrm{p}$. The user can now specify the vertical and horizontal permeabilities ($\mathrm{k_{p,v}}$, $\mathrm{k_{p,h}}$) which are the components of the initial, diagonal tensor $\mathbf{K}_{\mathrm{p0}}$. The tensor in current configuration $\mathbf{k}_\mathrm{p}$ results according to Eq. (24) and thus rotates and scales with the deformed soil.

4.1 Consolidation of an elastic finite soil layer

In order to validate the modification of the code, the method is compared to the analytical solution for consolidation problems in multi-layered half space with anisotropic permeability by Chen (2004).

The test case consists of a homogenous, fully saturated, elastic soil layer on a rigid, rough and impermeable bedding. The thickness of the layer equals H while the horizontal/radial extension is infinite and thus free drainage is assumed. The load q on the layer is circular with the radius $\mathrm{a} = \mathrm{H}$ and a magnitude of 1 (see Fig. 4).

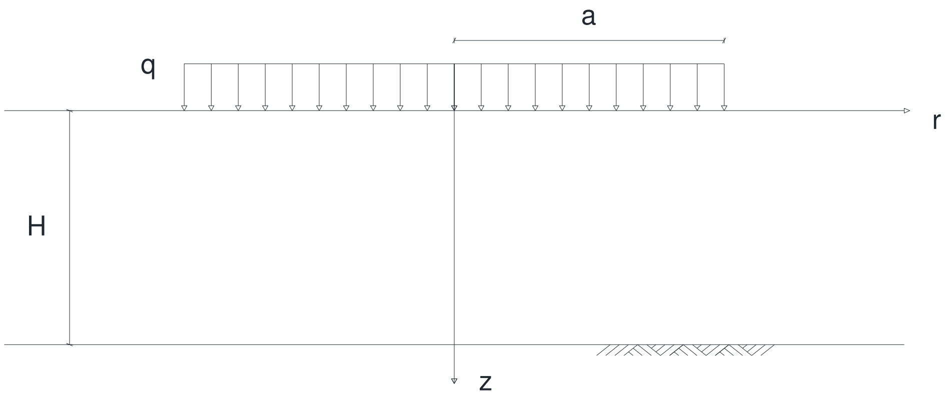

Fig. 4 Model of axisymmetric elastic soil layer on rigid, rough and impermeable base.

Based on given $\mathrm{K_w}$, Poisson's ratio ν and permeability ratios $\gamma^2 = \mathrm{k_{p,h}}/\mathrm{k_{p,v}}$, Chen (2004) provides dimensionless solutions for the surface subsidence and pore water pressures as functions of space and time. So, the dimensionless surface settlement $\mu \mathrm{w(r,z,T)/qa}$ at the centre point of the domain ($\mathrm{r = z = 0}$), is expressed depending on the dimensionless time factor $\mathrm{T = k_v \mu t/a^2}$, with μ being the material shear modulus. The dimensionless pore water pressure $\mathrm{p/q}$ is given as a function of the normalized depth

z/H at certain time steps T. In G-PFEM an axisymmetric model is built with a depth of 1 m and a horizontal model size of 5 m. The soil and pore water is assumed to be weightless, whereas a load of 10 Pa is applied. Tab. 1 summarizes the used material parameters.

Tab. 1 Input parameters for elastic soil layer in consolidation example.

ρ_s [kg/m³]	ρ_w [kg/m³]	ν [-]	μ [Pa]	K_w [Pa]	$k_{p,v}$ [m²/(Pa s)]
0	0	0.25	$4*10^5$	$4.5*10^{10}$	$1*10^{-7}$

The calculations are performed for a range of $\gamma^2 = (0.01, 1, 10, 100)$. Fig. 5 shows the dimensionless settlement as a function of the time factor suggesting good qualitative behaviour of the numerical calculations (which are given as piecewise linear functions between the functional values at different time steps). In agreement with the analytical solution, the displacement increases by time, starting from an instantaneous settlement until reaching a final, consolidated level. Due to the imposed drainage boundary conditions, radial (horizontal) flow is predominant. Thus, the higher the horizontal permeability is, the faster the final settlement is reached. The G-PFEM calculations reproduce this pattern, whereby the amount of instantaneous and final settlement is lower by around 3 to 7 % compared to the analytical solution.

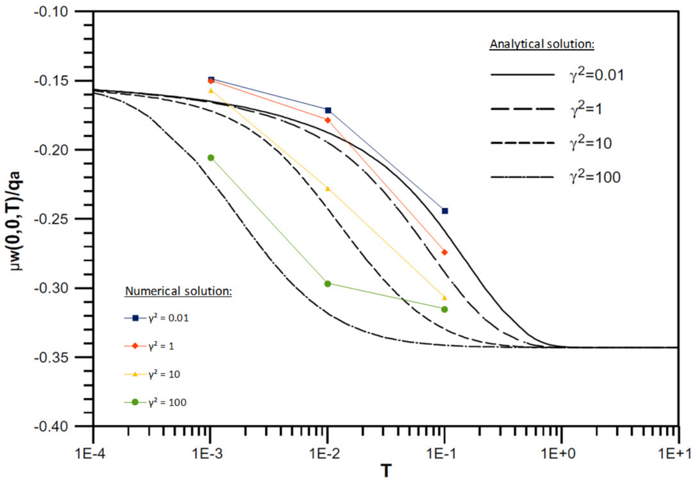

Fig. 5 Comparison of normalized displacement at centre point $(r = z = 0)$ versus time factor T for different permeability ratios γ^2 (Chen 2004).

The generated excess pore pressure is examined in Fig. 6 and the numerical results show good overall agreement with the analytical solution. Again, a high permeability ratio means faster drainage resulting in accelerated decay of the excess pore pressure. The pressure at the top of the soil layer is 0 since free drainage takes place. For small T, the pore pressure curves have a steep gradient at the surface which is followed by a peak. With increasing time the peak disappears and the pressure increases monotonically until reaching the maximum value at the impervious bottom. Eventually, the curve flattens out as the pore pressure decreases with time.

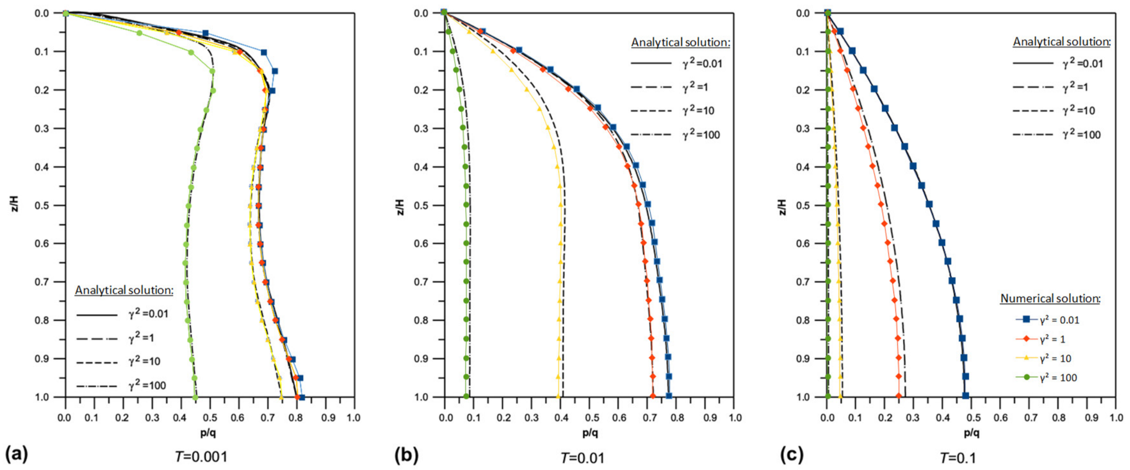

Fig. 6 Comparison of normalized pore pressure p/q versus dimensionless depth z/H along the symmetry axis at given instances of time T (Chen 2004).

4.2 Summary

Introducing anisotropic permeability can be a useful extension of G-PFEM allowing to model natural soil deposits in a more realistic way. A first benchmark for an elastic soil layer provides promising results.

5 Numerical simulation of CPTu

Equipped with the necessary numerical computation tool, the investigation of the soil behaviour during CPTs is the main subject of the following numerical examples. Initially, the 'on-the-fly' method by Chai et al. (2011), linking measured pore pressure to hydraulic conductivity of the soil, was investigated in order to get familiar with G-PFEM. Subsequently, a section of an actual CPTu sounding was recalculated and compared to the in-situ measurements. Based on this model further calculations were conducted considering varying penetration velocities and higher permeability allowing to investigate the soil behaviour for partial drainage around the cone. Finally, the deformation behaviour of silts during CPT was examined and compared to small scale experiments.

5.1 Determination of hydraulic conductivity from CPTu

The determination of the hydraulic conductivity k of a soil deposit is an important task in every geotechnical project as it represents a crucial parameter for analyzing the hydraulic behaviour. Therefore, Chai et al. (2011) presented an 'on-the-fly' method for estimating k from CPTu measurements without performing consolidation tests. The authors calibrated their semi-empirical approach based on a set of laboratory tests of Japanese Ariake clays and finally suggested a range of applicability for normally to slightly overconsolidated clays and loose sandy deposits.

The goal of this study is to learn the way of modelling CPTu with G-PFEM and at the same time validate the proposed method. Initially, the basic ideas behind the 'on-the-fly' method are pointed out.

5.1.1 'On-the-fly' method

The authors pick up the work of Elsworth & Lee (2005) considering the insertion of a cone in a soil body and introduce some modifications: Firstly, the displaced volume per time $\Delta\dot{\mathrm{V}}$ is assumed to be directly proportional to the resulting half-spherical water flow $\mathrm{q}_{\mathrm{flow}}$ giving

$$\begin{aligned} \Delta\dot{V} &= q_{flow} \\ \pi\, R^2\, U &= 2\pi\, R^2\, v_R \end{aligned} \tag{44}$$

with the cone radius R, the penetration velocity U and the water flow velocity v_{R} at the cavity (radial distance R from the centre axis). The latter may be expressed by Darcy's law as $\mathrm{v}_{\mathrm{R}} = \mathrm{k}\,\mathrm{i}_{\mathrm{R}}$ where the hydraulic conductivity k has the unit m/s.

The second basic assumption involves the water pressure distribution around the cavity. The generated excess pore pressure $\Delta \mathrm{u_R}$ is maximal at the radial distance R from the centre axis and equal to zero at an infinite distance. This partially drained condition implies that the permeability of the soil is low enough to allow the generation of excess pore pressure but still high enough for the occurrence of 'dynamic steady' flow, as suggested by Chai et al. (2011).

Darcy's law is rewritten with the hydraulic gradient $\mathrm{i_R}$ being a function of $\Delta \mathrm{u_R}$, γ_w and R:

$$v_R = k \frac{\Delta u_R}{\gamma_w \, R} \tag{45}$$

Combining Eq. (44) and Eq. (45) allows to express the hydraulic conductivity as

$$k = \frac{U \, R \, \gamma_w}{2 \, \Delta u_R} \tag{46}$$

Finally, the dimensionless expressions for the tip resistance $\mathrm{Q_t}$ and the pore water pressure ratio $\mathrm{B_q}$ are introduced as

$$\begin{gathered} Q_t = \frac{q_t - \sigma_{v0}}{\sigma'_{v0}} \\ B_q = \frac{\Delta u_R}{q_t - \sigma_{v0}} \end{gathered} \tag{47}$$

where $\mathrm{q_t}$ stands for the corrected tip resistance. At this point, the authors define the dimensionless hydraulic conductivity index:

$$K_D = \frac{1}{B_q \, Q_t} \tag{48}$$

$$\frac{2 \, k \, \sigma'_{v0}}{R \, \gamma_w \, U} = \frac{\sigma'_{v0}}{\Delta u_R} \tag{49}$$

Note that for the elaborated case of partial drainage Eq. (48) is independent of the mechanical soil properties and the permeability is assumed isotropic for the derivation.

Based on laboratory tests of Japanese clays, the authors corrected the relation for the range of $\mathrm{B_q \, Q_t} > 0.45$ by introducing the empirical correction factors $\alpha = 0.044$ and $\beta = 4.91$. This results in an updated version of Eq. (48):

$$K_D = \frac{\alpha}{\left(B_q\, Q_t\right)^{\beta}} \tag{50}$$

Note that the used hydraulic conductivity represents $\mathrm{k_h}$. The proposed bi-linear relation by Chai et al. (2011) is illustrated in Fig. 7.

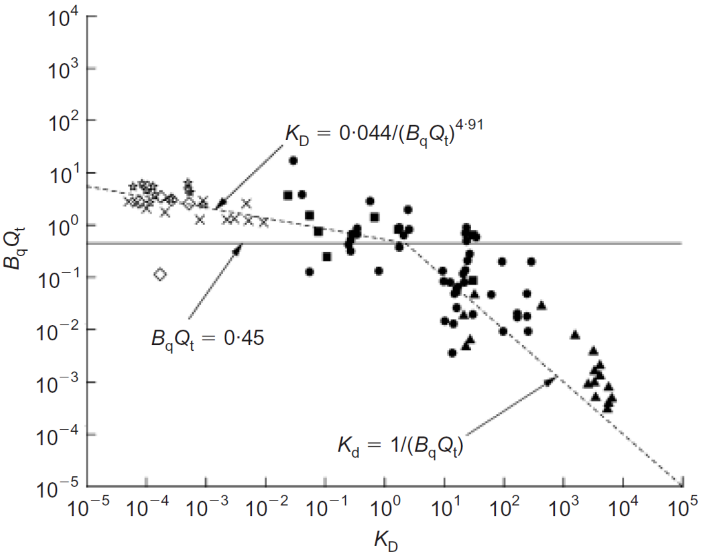

Fig. 7 Proposed bi-linear $K_D - B_q\, Q_t$ relationship with modified data points from Elsworth & Lee (2007) taken from Chai et al. (2011).

5.1.2 Numerical calculations

A set of calculations is carried out in order to investigate the proposed relation. Thereby, the effects of changing penetration velocities and a variation of initial, vertical stress σ'_{v0} are of main interest.

The problem domain is defined as a rectangular box with b = 0.45 m and h = 0.9 m and is axisymmetric with respect to the y-axis. The penetrating cone has a tip angle α_c of 60° and a base radius R of 1.78 cm which corresponds to standard geometry. At time $t = 0$ the cone is already located in the soil with its tip at a depth of h_1 = 0.1 m. The domain's lateral and lower boundaries are fixed in normal direction while water can drain freely except along the symmetry axis. The model is illustrated in Fig. 8 and serves as basis for all following calculations.

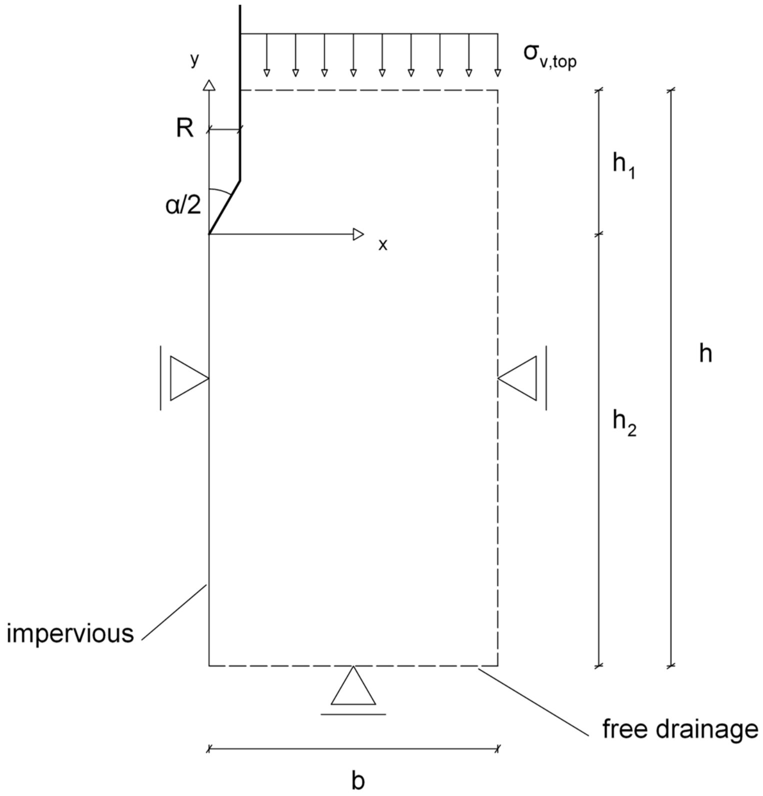

Fig. 8 Axisymmetric model of the domain.

The soil is modelled using a MCC model (see Tab. 2) based on the test case from Monforte et al. (2016). Initially, constant and equal stress fields, both for the effective soil stresses and the pore water pressure, are assumed. Thereby, $\sigma'_{\mathrm{v,top}}$ and $\mathrm{p_{w,top}}$ vary between 10, 50 and 100 kPa, resulting in the total vertical stress $\sigma_{\mathrm{v,top}}$ of 20, 100 and 200 kPa. The penetrometer is pushed with two different penetration velocities ($\mathrm{U_1}$ = 2 cm/s for case (a) and $\mathrm{U_2}$ = 1 cm/s for case (b)) around 0.4 m into the soil while recording the pore pressure at the shoulder position $\mathrm{u_2}$. No friction along the cone is considered.

Tab. 2 MCC input parameters for silty sand.

ρ_s [t/m³]	ρ_w [t/m³]	λ^* [-]	κ^* [-]	ϕ' [°]	M [-]
0	0	0.0685	0.0137	27	1.07

OCR [-]	G_0 [kPa]	α [-]	p_{c0} [kPa]	$k_{p,iso}$ ($k_{p,h}$) [m²/(kPa s)]	K_0 [-]
1	400	40	100	$1*10^{-7}$	0.7

The excess pore pressure Δu_2 results after subtracting the constant initial pressure p_{w0} and is plotted against the dimensionless depth in Fig. 9. Apart from two base cases with isotropic permeability and changing penetration velocities, a third case (c) was investigated considering anisotropic permeability. Thereby, the vertical one is reduced to $k_{p,v}$ = 0.5 $k_{p,h}$ while $k_{p,h}$ = $k_{p,iso}$. Each excess pore pressure curve appears to reach a stationary level after an initial build-up which is also expected for a constant initial stress field and weightless constituents. Note that oscillations increase at higher initial stress state. In order to get the computations running a stepwise decrease of the penalty weight with increasing initial stresses was necessary. This could however contribute to the intensified oscillatory behaviour. In Fig. 9 (b) a jump in Δu_2 is evident which has no physical meaning but is rather a numerical issue.

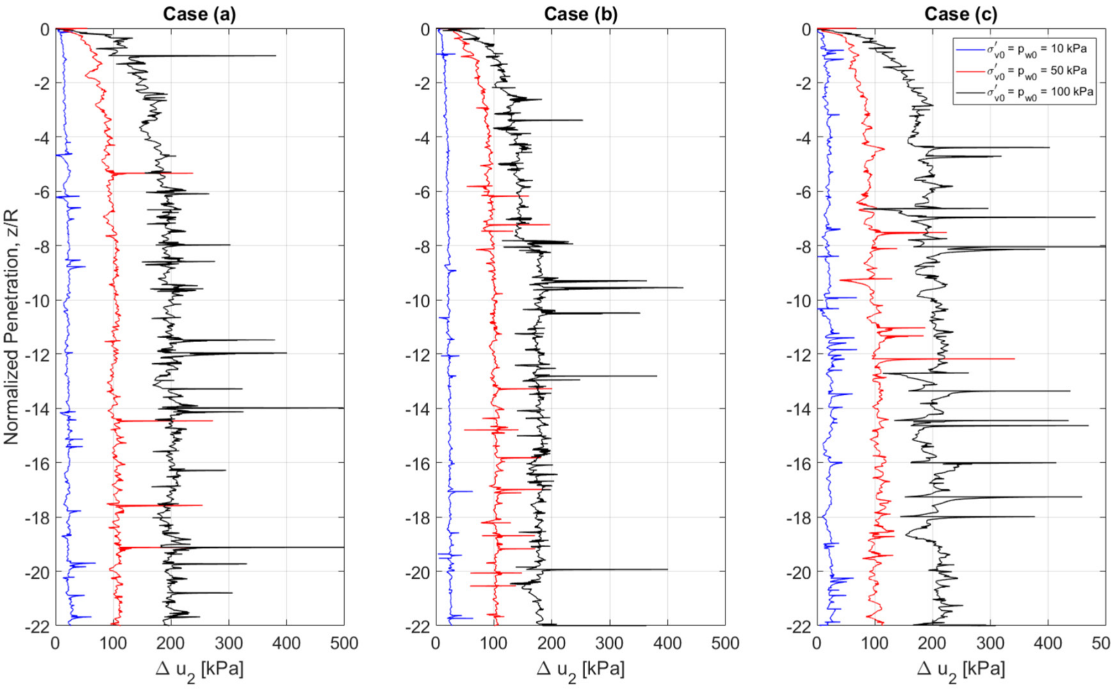

Fig. 9 Computed excess pore pressure Δu_2 versus normalized depth for varying penetration velocities, both isotropic and anisotropic permeabilities and changing initial stress conditions.

Based on the Δu_2-curves from Fig. 9, mean values of Δu_2 at different depths are calculated and summarized in Tab. 3. Thereby, the initial effective stresses and pore pressures of 10, 50 and 100 kPa correspond to overburden depths of 1, 5 and 10 m respectively. Eventually, the proposed 'on-the-fly' method is used allowing to estimate the hydraulic conductivity as a function of Δu_2, σ'_{v0}, U, R, γ_w and the correction factors α, β. The resulting values for $B_q * Q_t$ vary between 1.77 and 2.4 and are clearly larger than 0.45. Hence, the semi-empirical approach according to Eq. (50) applies and the resulting 'on-the-fly' hydraulic conductivities are given in Tab. 3. It appears reasonable that cases (a) and (c) provide almost the same results since radial (or horizontal) flow is the dominating mode and the reduced vertical permeability has little impact. Case (b) gives almost identical excess pore pressures compared to cases (a) and (c), except for a depth of 10 m where the observed jump in the distribution has major influence. However, according to the proposed method, lower penetration velocities should result in lower $\Delta\bar{u}_2$ in order to obtain the same value for k. The back-calculated 'on-the-fly' conductivities vary between $2.1*10^{-8}$ and $1.6*10^{-7}$ m/s which gives an overall mean value of $5.8*10^{-8}$ m/s, around 17 times lower than the input value of $1*10^{-6}$ m/s.

Tab. 3 Mean excess pore pressure $\Delta\bar{u}_2$ and resulting 'on-the-fly' hydraulic conductivity k_{otf} at different depths.

Values (at different depths)		**Case (a)** **U_1, $k_{p,iso}$**	**Case (b)** **U_2, $k_{p,iso}$**	**Case (c)** **U_1, $k_{p,v} = 0.5*k_{p,h}$**
$\Delta\bar{u}_2$ [kPa]	1 m	22	24	23
	5 m	106	104	106
	10 m	202	177	205
k_{otf} [m/s]	1 m	$1.6*10^{-7}$	$5.3*10^{-8}$	$1.3*10^{-7}$
	5 m	$3.9*10^{-8}$	$2.1*10^{-8}$	$3.9*10^{-8}$
	10 m	$2.5*10^{-8}$	$2.4*10^{-8}$	$2.3*10^{-8}$
	mean	$7.6*10^{-8}$	$3.3*10^{-8}$	$6.4*10^{-8}$

Finally, the results are also illustrated in a double logarithmic $K_D - B_q\,Q_t$ plot next to the proposed bi-linear relation in Fig. 10. Thereby, the values for K_D are calculated based on the input hydraulic conductivity and plotted against the corresponding $B_q\,Q_t$. The cloud of points is located within reasonable range to the corrected branch of the bi-linear relation. Furthermore, the piecewise linear connection for each case shows a similar trend compared to the proposed solution.

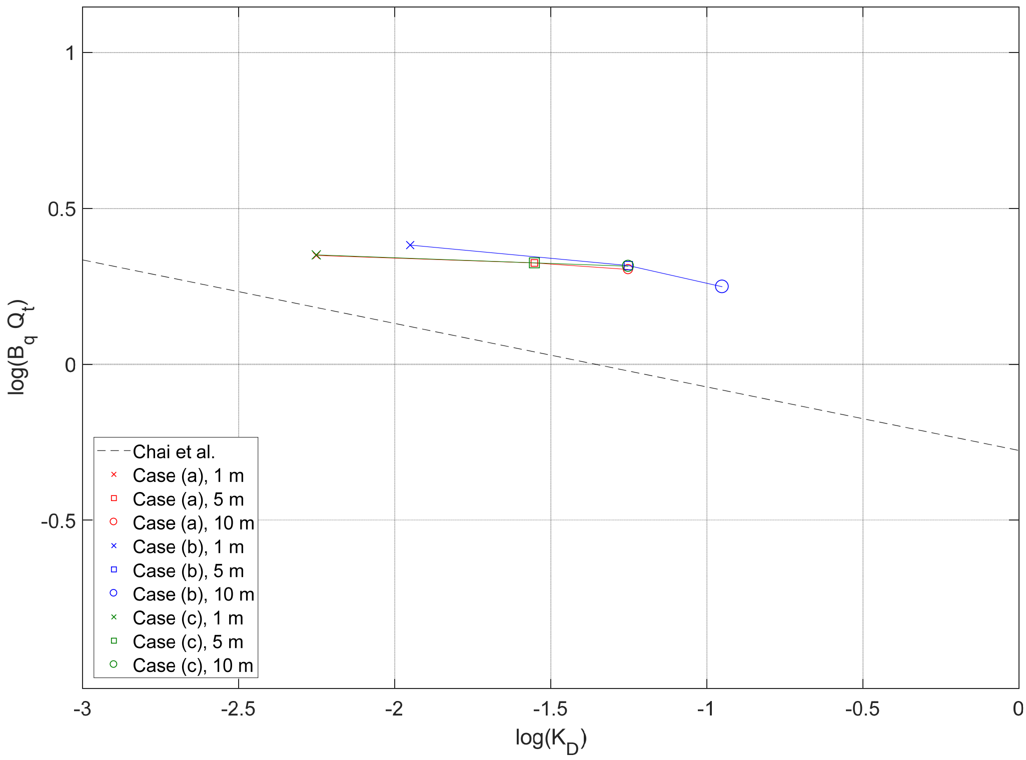

Fig. 10 Double logarithmic plot of resulting $\Delta\bar{u}_2$ in terms of K_D and $B_q Q_t$ for the cases (a) to (c) at depths of 1, 5 and 10 m.

5.1.3 Summary

For the examined cases, where a silty sand was considered, the ‘on-the-fly’ method estimates lower permeablities. However, the method appears to be useful for a first estimation of k, especially under partially drained conditions. The work so far showed that numerical simulation of CPTs provides comparable results, so further investigations can play an important role for determining the limits of applicability of the proposed relation, especially since mechanical soil properties play no role in the analytical derivation of the method.

5.2 Recalculation of in-situ CPTu

In his Master's thesis, Sachsenhofer (2012) discusses various in-situ CPTu tests and derives material parameters from the measurements. Based on both, the available soil parameters and the CPTu profiles in terms of tip resistance q_c, sleeve friction f_s and pore pressure at the shoulder position of the cone u_2, the penetration process through a clayey to silty layer is simulated with G-PFEM. The soil parameters are averaged over a 5 m thick layer situated a 13 to 18 m depth, while the in-situ water table is located at a depth of 3 m. The hydraulic conductivity is taken for 'Salzburger Seeton' and Poisson's ratio is set to 0.3. The basic parameters are summarized in Tab. 4.

Tab. 4 Input parameters for clayey to silty soil layer averaged over 5 m thick layer.

γ_s [kN/m³]	ϕ' [°]	E_s [kPa]	ν [-]	k_v [m/s]	σ'_{v0} [kPa]
17	22.5	$1*10^4$	0.3	$2*10^{-8}$	150

Subsequently, the G-PFEM model is built based on Fig. 8: Thereby, the domain measures 1.1 m of height (with h_1 and h_2 being 0.1 or rather 1.0 m) times b equal to 0.5 m. Again, the lateral and lower boundaries are fixed in normal direction and free drainage is assumed except along the symmetry axis. A standard cone is used with R equal to 1.78 cm and α_c of 60°. The vertical load on top of the domain $\sigma_{v,top}$ is set to 230 kPa according to the overburden and water table position ($\sigma'_{v,top}$ = 130 kPa, $p_{w,top}$ = 100 kPa). The initial stress state is computed as a gravitational loading. The initial mesh size and adaptive refinement parameters are based on Monforte et al. (2016).

5.2.1 Calculation 1: CPTu with rough and smooth cone

The use of the MCC model requires the calculation of relevant model parameters based on the material parameters from Tab. 4. Thereby, the stiffness parameters λ^*, κ^* and G_0 are calculated from E_s, ν and σ'_{v0} according to the theory of elasticity. K_0 and M depend on ϕ' while the anisotropy ratio between vertical and horizontal permeability is assumed 10. The base case considers a rough cone with a contact friction angle $\phi_{contact} \approx \phi'/3$ whereby an alternative calculation is performed with a smooth cone in order to investigate the difference. The resulting model parameters are summarized in Tab. 5. The calculations are carried out until a penetration depth of around 0.45 m is reached. Initially, the focus lies on assessing the quality of the computation with regard to the stabilization of the problem. Fig. 11 shows the contour plots for the computed nodal

Jacobian Θ (a) and the water pressure p_w (b) around the rough cone at a penetration depth of around 22 cm. The spherical distributions are smooth and do not exhibit oscillatory behaviour, even for the almost incompressible system behaviour with the Jacobian ranging between 0.994 and 1.00054.

Tab. 5 Calculation 1: MCC input parameters for clayey/silty soil layer.

ρ_s [t/m³]	ρ_w [t/m³]	λ^* [-]	κ^* [-]	ϕ' [°]	M [-]	G_0 [kPa]	α [-]
1.7	1	0.015	0.005	22.5	0.88	$2.9*10^3$	0

OCR [-]	p_{c0} [kPa]	K_w [kPa]	$k_{p,v}$ [m²/(kPa s)]	$k_{p,h}$ [m²/(kPa s)]	K_0 [-]	$\phi_{contact}$ [°]	e_0 [-]
1	100	$1*10^8$	$2*10^{-9}$	$2*10^{-8}$	0.7	7 (0)	0.5

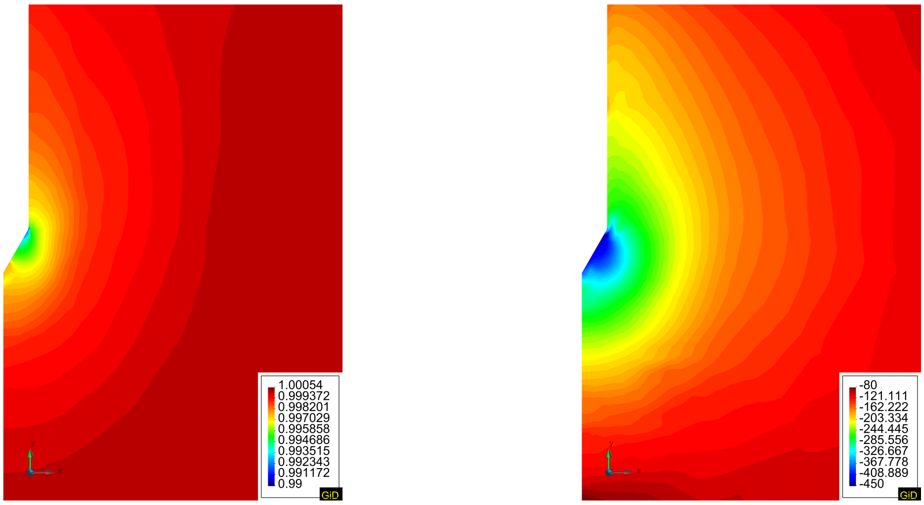

(a) (b)

Fig. 11 Calculation 1 – rough cone: Contour plots of nodal Jacobian Θ [-] (a) and the water pressure $\mathrm{p_w}$ [kPa] (b) at a penetration depth of around 22 cm.

During the computation $\mathrm{q_c}$, $\mathrm{f_s}$ and $\mathrm{u_1}$, $\mathrm{u_2}$, $\mathrm{u_3}$ are recorded for each step and plotted against the dimensionless depth $\mathrm{z/R}$ (see Fig. 12). Apart from the oscillations of $\mathrm{u_2}$, the results show smooth behaviour. After an initial 'transient phase' the measured quantities seem to reach a stationary level where only a slight increase due to the gravitational initial stress field is observed. This applies also to the overall behaviour of $\mathrm{u_2}$ where the measured total pore pressure oscillates around a stationary level. Note that the contact friction angle is gradually increased during the computation in order to minimize computational instability which explains the apparent longer 'transient phase' of $\mathrm{f_s}$. The difference between a rough and smooth cone is small for the defined degree of contact friction. This is a helpful information with regard to further calculations since tangential contact forces on the interface due to friction require the introduction of a tangential penalty factor as an additional numerical parameter.

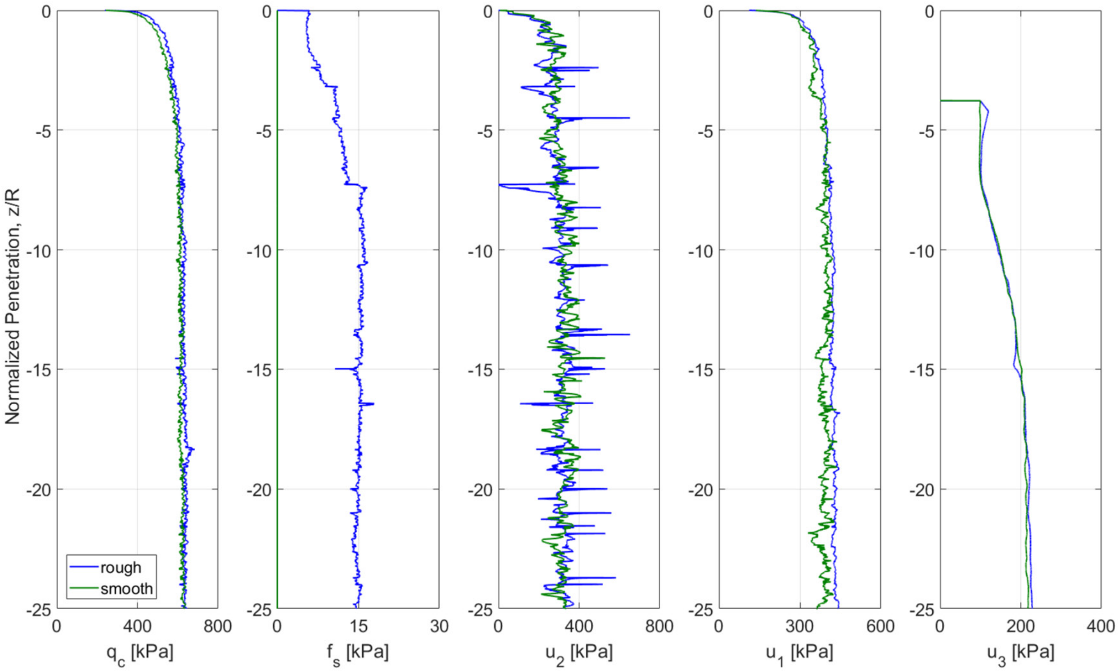

Fig. 12 Calculation 1: CPTu log of recalculated in-situ test with smooth and rough cone.

Since the available in-situ CPTu data does not provide comparable logs on this small scale the recalculation is validated by comparing the computed mean values to the measured in-situ values at a depth of 13 to 14 m (see Tab. 6). The computed mean and the measured in-situ values for the tip resistance and the sleeve friction show the same order of magnitude and therefore suggest good agreement. However, the computed pore water pressure is higher than the measured one, roughly by a factor of 10. So, the in-situ hydraulic conditions appear not to be correctly captured within the model.

Tab. 6 Calculation 1: Comparison of calculated and measured values for q_c, f_s and u_2.

Values		**G-PFEM rough cone** (mean value)	**In-situ CPTu** (measured order of magnitude)
q_c	[kPa]	635	800
f_s	[kPa]	15	20
u_2	[kPa]	320	35

5.2.2 Calculation set 2: Impact of varying penetration velocity

In order to gain a better understanding of the hydraulic behaviour during cone penetration tests the calculation is performed for different penetration velocities v_c. The faster the cone is pushed into the soil the closer one gets to undrained loading conditions and thus higher pore pressures are expected to be generated. Interestingly, Fig. 13 shows no qualitative difference between the examined cases suggesting that the combination of (low) permeability and penetration velocities of 1 to 3 cm/s is creating almost undrained behaviour. The generated pore pressure is therefore treated as a maximum undrained pressure.

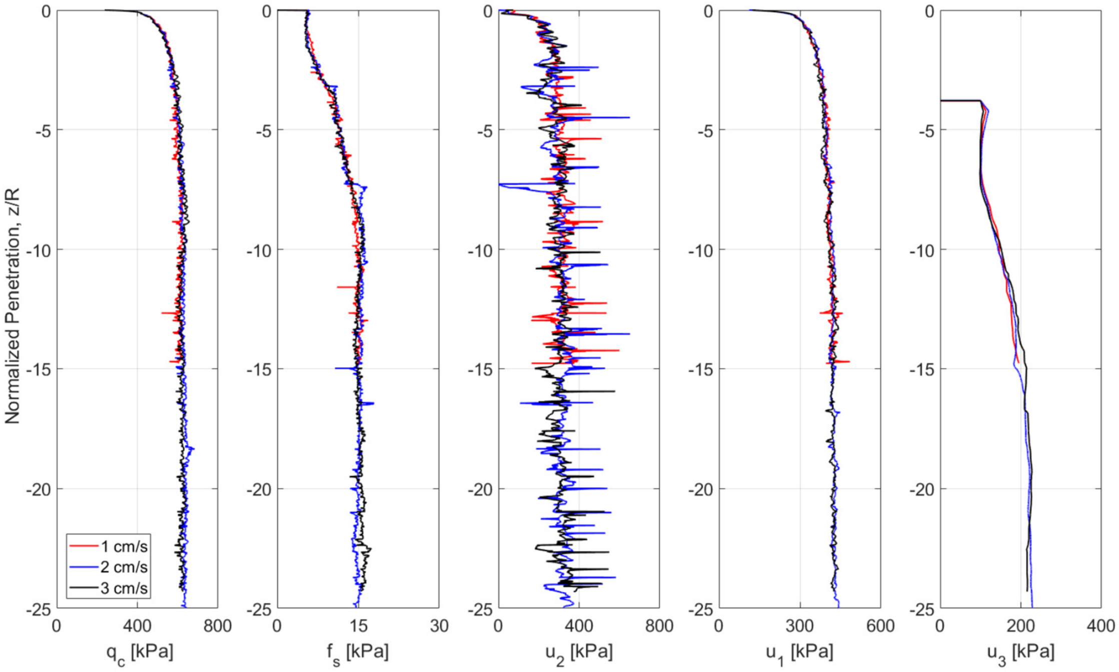

Fig. 13 Calculation set 2: CPTu log for varying penetration velocities with rough cone.

A similar value for the pore pressure can be found with the analytical approach by Burns & Mayne (1998). Thereby, the excess pore pressure is divided into a normal- and shear-induced component. The former is derived from cavity-expansion theory while the latter relies on the MCC model. Thus, the undrained pore pressure at $t = 0$ yields

$$u_m = \frac{4}{3}\left[\sigma'_{v0}\frac{M}{2}\left(\frac{OCR}{2}\right)^{\Lambda}\right]\ln I_r + \sigma'_{v0}\left[1-\left(\frac{OCR}{2}\right)^{\Lambda}\right] + u_0 \qquad (51)$$

with the plastic volumetric strain ratio $\Lambda = 1 - C_s/C_c$, the rigidity index $I_r = G/s_u$ and the initial water pressure u_o. Λ, which depends on the swelling and compression indices, is typically 0.8 for natural clays (Burns & Mayne 1998).

For the present case, u_m results in around 350 kPa showing the same order of magnitude as the computed mean values from Tab. 7.

Tab. 7 Calculation set 2: Results of calculated values (q_c, f_s, u_2) for varying penetration velocities.

G-PFEM (mean value)		**v$_c$ = 1 cm/s**	**v$_c$ = 2 cm/s**	**v$_c$ = 3 cm/s**
q_c	[kPa]	610	635	620
f_s	[kPa]	15	15	15
u_2	[kPa]	315	320	310

Moreover, Fig. 14 shows the Darcy flow for the three different test cases after roughly 22 cm of penetration. No substantial differences are evident for the variation of penetration velocity, neither qualitatively nor quantitatively. The maximum flow is less than 0.0009 m/s and the flow pattern appears to be independent of time since cones with different velocities reach the same penetration depth at different time instances. This makes sense for undrained conditions where the soil-water body behaves as a single phase medium and thus no relative flow occurs, in other words the Darcy flow is zero.

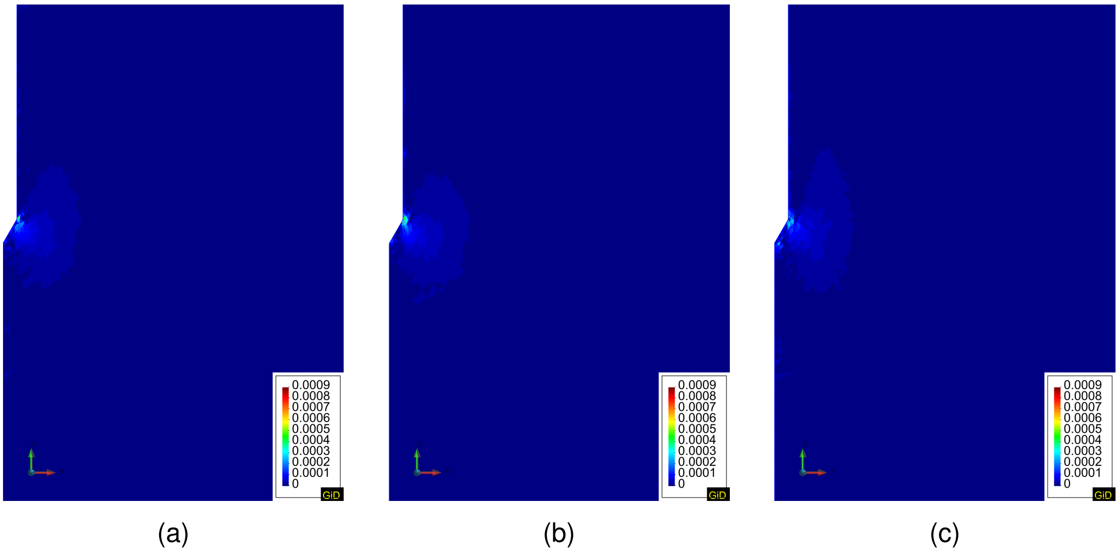

(a) (b) (c)

Fig. 14 Calculation set 2: Contour plots of the magnitude of Darcy flow [m/s] for penetration velocities of 1 cm/s (a), 2 cm/s (b) and 3 cm/s (c) at a penetration depth of 22 cm.

5.2.3 Calculation set 3: Partially drained conditions during CPT

Subsequently, the main objective is to create partially drained conditions where local flow takes place but significant excess pore pressures are still generated. Therefore, increased isotropic permeability is assumed while the cone surface is set smooth in order to achieve more stability during the computation. The input parameters are summarized in Tab. 8. Again, the calculation is carried out for different penetration velocities v_c of 1, 2 and 3 cm/s.

Tab. 8 Calculation set 3: MCC input parameters for clayey to silty layer.

ρ_s [t/m³]	ρ_w [t/m³]	λ^* [-]	κ^* [-]	ϕ' [°]	M [-]	G_0 [kPa]	α [-]
1.7	1	0.015	0.005	22.5	0.88	$2.9 \cdot 10^3$	0

OCR [-]	p_{c0} [kPa]	K_w [kPa]	$k_{p,iso}$ [m²/(kPa s)]	K_0 [-]	$\phi_{contact}$ [°]	e_0 [-]
1	100	$1 \cdot 10^8$	$2 \cdot 10^{-7}$	0.7	0	0.5

Compared to calculation set 2, the overall water pressure level is lower while the tip resistance increases (see Tab. 9). This appears reasonable for increased permeability and consequently increased drainage as more load is carried by the soil skeleton instead of having an undrained single-phase behaviour. Considering the displacement-controlled nature of CPT, higher tip resistances are a plausible consequence. Furthermore, partial drainage manifests in the form of observable differences in tip resistance and pore pressure for varying penetration velocities.

Tab. 9 Comparison of calculated mean values of q_c and u_2 of calculation sets 2 and 3 for varying penetration velocities.

G-PFEM (mean value)		**v_c = 1 cm/s**	**v_c = 2 cm/s**	**v_c = 3 cm/s**
q_c [kPa]	Calc 2	610	635	620
	Calc 3	730	775	720
u_2 [kPa]	Calc 2	315	320	310
	Calc 3	195	205	255

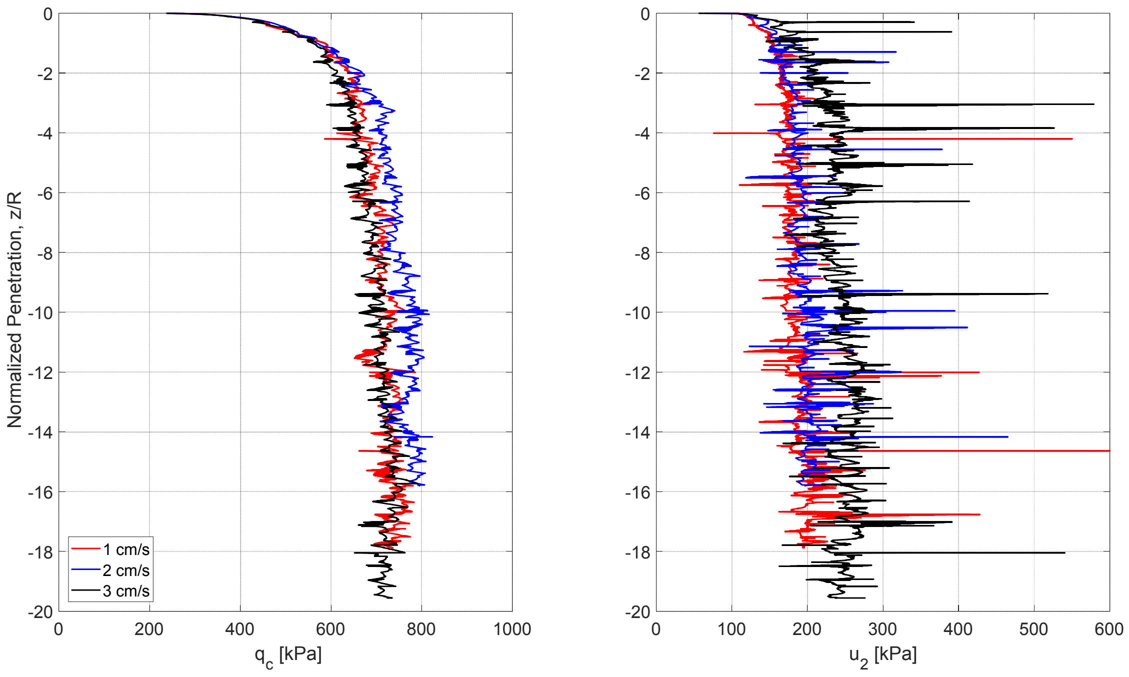

Fig. 15 Calculation set 3: CPTu log for varying penetration velocities with smooth cone.

The corresponding CPTu log is illustrated in Fig. 15 showing increased oscillations of the water pressure around the stationary level. Increased drainage results in increased volumetric deformation. This requires different stabilization of the problem compared to the almost undrained calculation set 2 in section 5.2.2. Fig. 16 shows smooth fields of the nodal Jacobians for all three penetration velocities after 22 cm of penetration. The highest velocity of 3 cm/s gives the least volume change as loading happens faster and less time for dissipation is available until reaching the given depth.

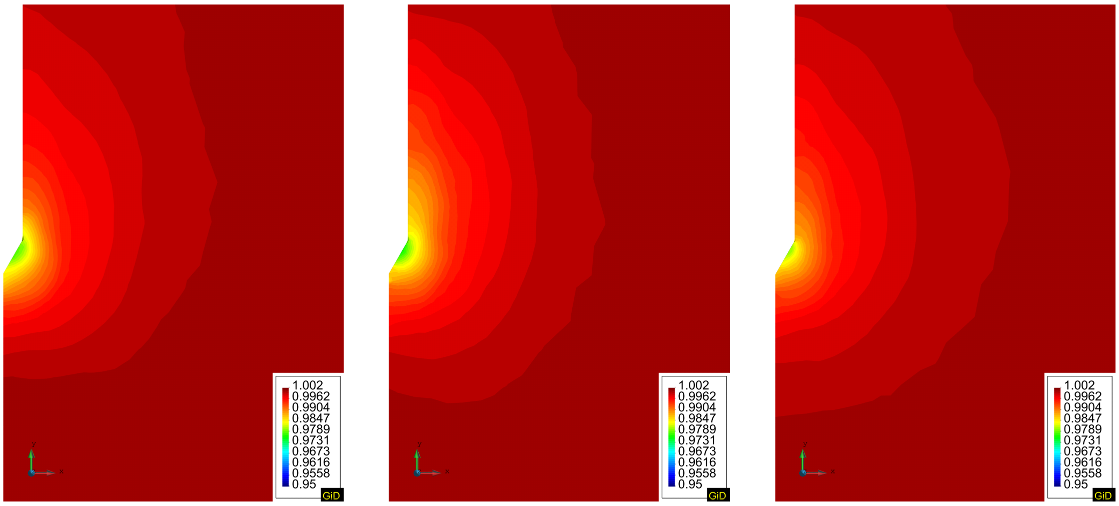

(a) (b) (c)

Fig. 16 Calculation set 3: Contour plots of nodal Jacobian Θ [-] for penetration velocities of 1 cm/s (a), 2 cm/s (b) and 3 cm/s (c) at a penetration depth of 22 cm.

When looking at $\mathrm{p_w}$ in Fig. 17, the same mechanism is observed as the fastest cone (c) builds up the highest pressures while slower loading (cases (a) and (b)) results in less excess pressure and more dissipation time until reaching 22 cm of depth. The pressure fields look smooth on a large scale, however, some local pressure fluctuations under the cone tip are observed, even more for cases (a) and (b).

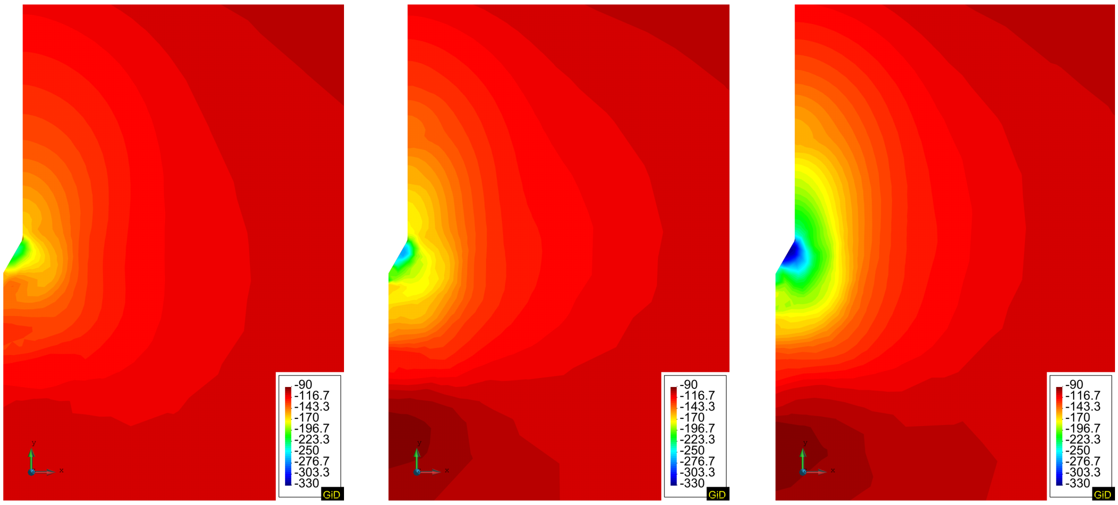

(a) (b) (c)

Fig. 17 Calculation set 3: Contour plots of water pressure $\mathrm{p_w}$ [kPa] for penetration velocities of 1 cm/s (a), 2 cm/s (b) and 3 cm/s (c) at a penetration depth of 22 cm.

In contrast to Fig. 14 in section 5.2.2, where almost no relative water flow is observable, a different flow pattern under partially drained conditions is illustrated in Fig. 18. Firstly, the order of magnitude is considerably higher compared to the almost undrained case (around 3 times) and secondly, clear differences for the variation of penetration velocity are evident. So consequently, slower penetration allows more dissipation and results in a smaller excess pore pressure 'bulb', or in other words, in a smaller region with flow. Increased velocity then gives higher water pressure and finally larger flow regions (see Fig. 18 (a) to (c)).

So far, the effects of changing penetration velocities under partially drained conditions appear consistent regarding the interaction of volume change, water pressure and water flow. Also, an increase of tip resistance makes sense since the soil starts to behave as frictional material to some extend instead of having constant shear strength under undrained conditions. Following the logic so far, increased penetration velocity means rather undrained condition and thus lower tip resistance. However, in the present case the highest tip resistance results for the intermediate penetration velocity (see Tab. 9 and Fig. 15). Numerical reasons behind this cannot be excluded at the moment and therefore additional computations are required. Anyway, deeper investigations on partial drainage are the upcoming steps in order to understand how the total measured stresses at the cone tip change as excess pore pressure dissipates and at the same time further load is applied by pushing the cone further down.

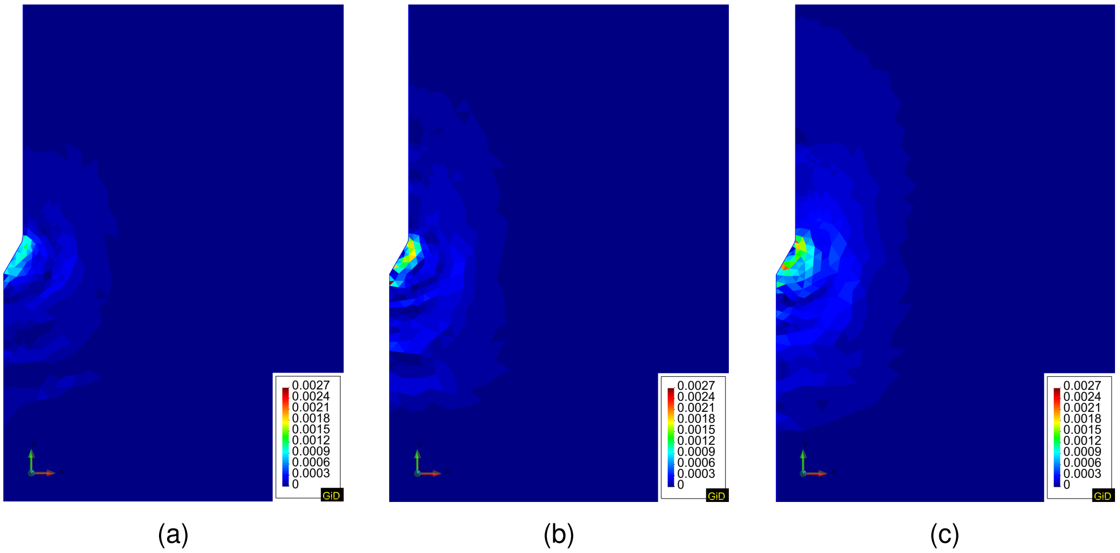

Fig. 18 Calculation set 3: Contour plots of the magnitude of Darcy flow [m/s] for penetration velocities of 1 cm/s (a), 2 cm/s (b) and 3 cm/s (c) at a penetration depth of 22 cm.

5.2.4 Summary

The comparison between the calculated and in-situ CPTu data shows good agreement since the values for q_c and f_s have the same order of magnitude, u_2 is still significantly higher. Also, modelling a rough cone which adds an additional numerical parameter to the problem seems to provide reasonable results. However, the hydraulic conditions which are primarily controlled by the permeability tensor are the crucial ingredient. The calculation sets show that G-PFEM provides plausible results both under almost undrained and partially drained conditions. The application is a powerful tool for studying partial drainage during CPTu.

Coming back to the initial recalculation of the in-situ CPTu, an increase of permeability led to reduced pore pressures whereby the in-situ measurement is still 5 to 6 times lower. Further investigations on the hydraulic behaviour of silts are the subject of the following section.

5.3 Behaviour of silts during CPTu

Paniagua et al. (2013) conducted small scale experiments on Norwegian silts and investigated incremental volumetric and shear strains. They found that both a compaction bulb and an expanding region develop around the cone as pointed out in Fig. 19. In this way, short drainage paths are formed as the water flows from the compacting into the expanding region explaining the low pore pressures around the cone.

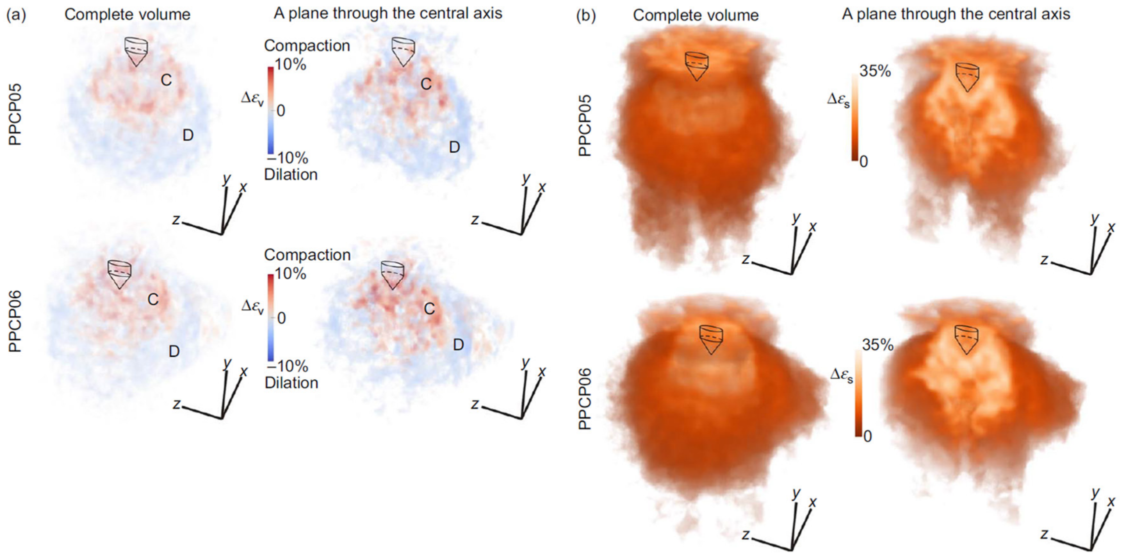

Fig. 19 Incremental volumetric strain $\Delta\epsilon_{\mathrm{vol}}$ (a) and shear strain $\Delta\epsilon_{\mathrm{shear}}$ (b) around the cone between 56 and 61 mm of penetration (Paniagua et al. 2013).

The mechanism of local drainage due to expansion and compaction is subject of the following section. Initially, the focus lies on investigating the soil behaviour in terms of incremental volumetric and shear strains. Eventually, the analysis of stress paths is expected to provide further information on the elasto-plastic response of the soil. Calculation set 3 with standard penetration velocity of 2 cm/s serves as basis for the following considerations.

5.3.1 Deformation behaviour around the cone

The incremental volumetric strain $\Delta\epsilon_{\mathrm{vol}}$ is calculated as post-processing from the nodal values of the Jacobian. Assuming the time instances t_1 and t_2 with the respective volumes V_1 and V_2, the incremental volumetric strain can be expressed dependent of the determinant of the incremental deformation gradient ${}_1^2\mathbf{F}$, which maps a line element from configuration t_1 to t_2:

$$\Delta\epsilon_{vol} = \frac{\mathrm{V}_2 - V_1}{V_1} = \frac{V_2}{V_1} - 1 = \det {}_1^2\boldsymbol{F} - 1 \tag{52}$$

A reference configuration t_0 is introduced allowing the formulation of the total deformation gradient and its determinant:

$$\begin{gathered} {}_0^2\boldsymbol{F} = \frac{dx_1}{dx_0}\frac{dx_2}{dx_1} = {}_0^1\boldsymbol{F}\ {}_1^2\boldsymbol{F} \\ \det {}_0^2\boldsymbol{F} = \det {}_0^1\boldsymbol{F} \cdot \det {}_1^2\boldsymbol{F} \\ {}_0^2J = {}_0^1J \cdot {}_1^2J \end{gathered} \tag{53}$$

Hence, $\Delta\epsilon_{\mathrm{vol}}$ is expressed depending on the Jacobians ${}_0^1\mathrm{J}$ and ${}_0^2\mathrm{J}$:

$$\Delta\epsilon_{vol} = \frac{{}_0^2J}{{}_0^1J} - 1 \tag{54}$$

Also, the incremental shear strain $\Delta\epsilon_{\mathrm{shear}}$ is a post-processing result based on the stepwise output of the Green-Lagrange strain tensor. The latter can be additively decomposed for different time steps (Bathe 2014) which gives:

$${}_0^2\boldsymbol{E} = {}_0^1\boldsymbol{E} + {}_0^\Delta\boldsymbol{E} \tag{55}$$

Then, the principal strains $\Delta\epsilon_1$, $\Delta\epsilon_2$ and $\Delta\epsilon_3$ are calculated for ${}_0^\Delta\mathbf{E}$ in order to obtain the incremental shear strain as computed in Paniagua et al. (2013):

$$\Delta\epsilon_{shear} = (2/3)^{1/2}[(\Delta\epsilon_1 - \Delta\epsilon_2)^2 + (\Delta\epsilon_2 - \Delta\epsilon_3)^2 + (\Delta\epsilon_3 - \Delta\epsilon_1)^2]^{1/2} \tag{56}$$

Note that in the mixed formulation the Jacobian is a nodal variable and thus approximated by piecewise linear functions while the Green-Lagrange strain is constant within an element. Consequently, the quality of $\Delta\epsilon_{\mathrm{vol}}$ is expected to be higher compared to $\Delta\epsilon_{\mathrm{shear}}$.

Referring to the work of Paniagua et al. (2013), $\Delta\epsilon_{\mathrm{vol}}$ and $\Delta\epsilon_{\mathrm{shear}}$ are calculated for a penetration increment of 5 mm starting at 3 different depths of 56 (a), 156 (b) and 256 (c) mm for calculation set 3 with standard penetration velocity of 2 cm/s. The computed $\Delta\epsilon_{\mathrm{vol}}$ is illustrated in Fig. 20 (a), (b) and (c): As observed in the experiments (Fig. 19 (a)), a clear compaction bulb below the cone and an expanding region at the shaft are obtained. Additionally, there is some local volumetric expansion centrically below the compacting zone which is most clearly manifested in Fig. 20 (c). This corresponds qualitatively to the observed experimental behaviour whereby the expanding zone is a local phenomenon and does not cover the whole compaction bulb as Fig. 19 (a) suggests. Furthermore, there are less compacted 'lenses' within the compaction bulb.

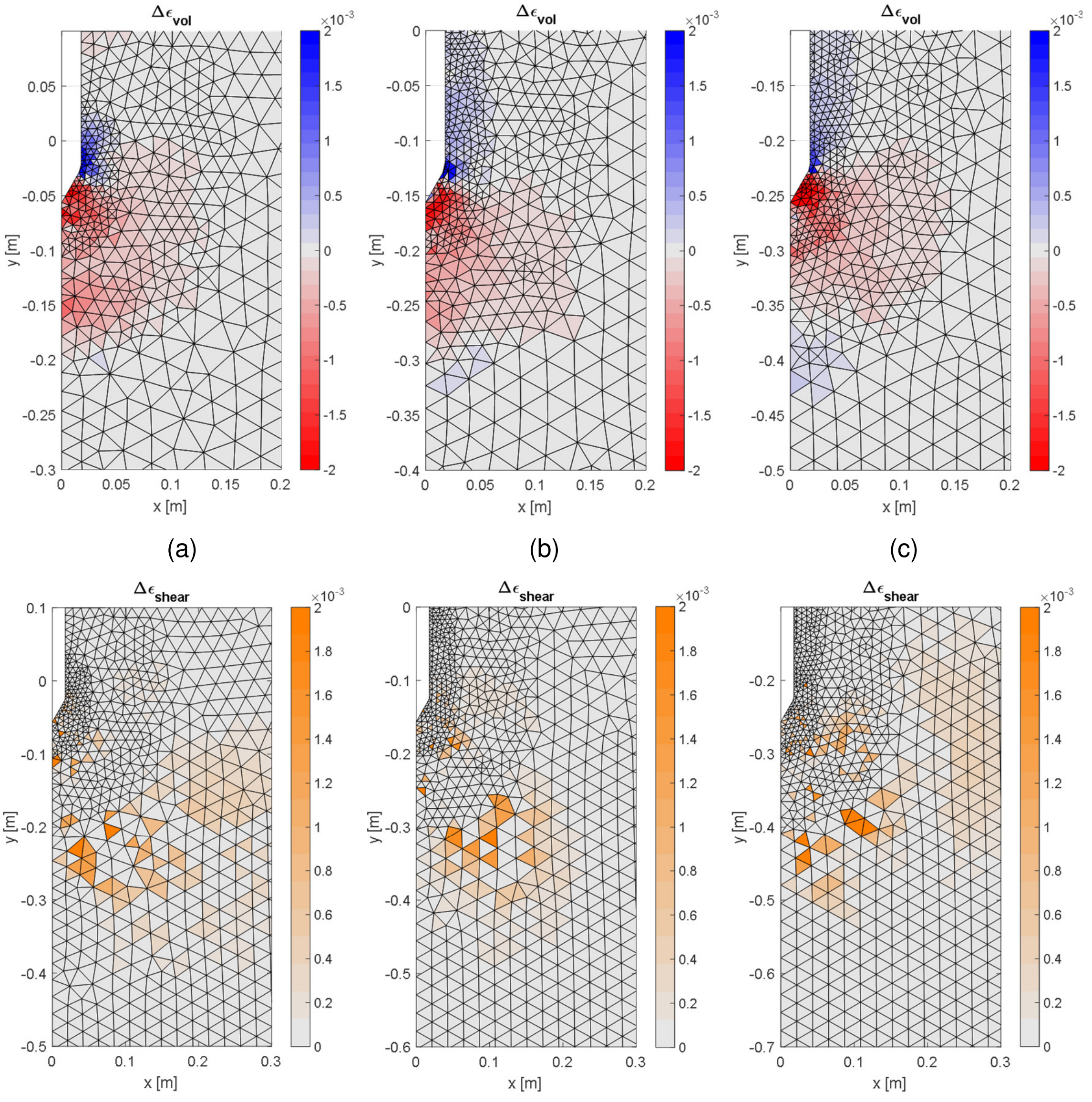

(a) (b) (c)

(d) (e) (f)

Fig. 20 Incremental volumetric strain $\Delta\epsilon_{\mathrm{vol}}$ and shear strain $\Delta\epsilon_{\mathrm{shear}}$ for the penetration increments 56 to 61 mm (a) & (d), 156 to 161 mm (b) & (e) and 256 to 261 mm (c) & (f) for calculation set 3 (isotropic, reduced permeability and v_c = 2 cm/s); volume increase is positive.

At the same time, the validation of $\Delta\epsilon_{\mathrm{shear}}$ is not as clear. In contrast to Fig. 19 (b), no distinct shearing zone around the cone is evident. Some shearing is observable at a radial distance of around 0.15 m below the cone, approximately at the transition from the initial coarse mesh to the already refined/remeshed region. This pattern holds true for all three penetration increments and is illustrated in Fig. 20 (d), (e) and (f). The interpretation of the computed $\Delta\epsilon_{\mathrm{shear}}$ is not obvious. Firstly, the shear strain measure is calculated based on the incremental Green-Lagrange strain tensor which might not correspond entirely to the derived strain measures from the experimental work. Secondly, the combination of the coarse mesh and the low order approximation of the strain quantities can also contribute to the difficulties in interpretation. Anyway, this issue requires additional work and therefore $\Delta\epsilon_{\mathrm{shear}}$ is not further considered.

Hence, the focus lies on investigating the observed volume change, especially whether the volume expansion is due to unloading or dilation: Initially, the pore pressure distribution is considered after 56, 156 and 256 mm of penetration (see Fig. 21). On a larger scale, the distributions appear reasonable as the initial excess pore pressure bulb at the cone tip (Fig. 21 (a)) travels down while increasing radial flow along the shaft of the penetrometer develops with time (see Fig. 21 (b) and (c)). The previously mentioned zone with volumetric expansion below the tip is also apparent in Fig. 21 (b) and (c) in the form of reduced pore pressure below the initial state of around -100 kPa. The resulting gradient causes local inward flow.

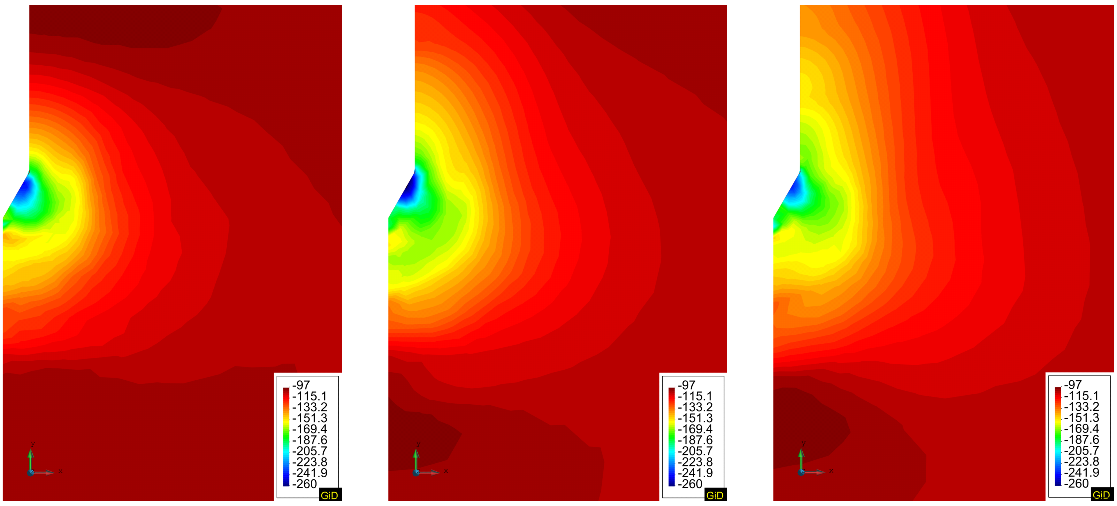

(a) (b) (c)

Fig. 21 Contour plots of pore pressure distribution $\mathrm{p_w}$ [kPa] around the cone after 56 mm (a), 156 mm (b) and 256 mm (c) of penetration.

Similar zones with reduced pore pressure and local inward flow can be found within the excess pore pressure bulb corresponding to the less compacted ‘lenses’ in the evaluation of $\Delta\epsilon_{\mathrm{vol}}$. The physical relevance of these local phenomena is questionable and can be interpreted as oscillations of the pressure field. Keeping this in mind, the incremental Jacobian $\Delta\Theta$ and the incremental plastic shear strain are evaluated at a penetration depth of 156 mm. Fig. 22 (a) indicates a compression bulb ($\Theta < 1$) containing expanding spheres ($\Theta > 1$). The spherical pattern, although based on a piecewise constant approximation, is also observable for the incremental plastic shear strain in Fig. 22 (b). Thereby, volumetric expansion ($\Theta > 1$) is associated with zero plastic shear strain suggesting that expansion is due to elastic unloading rather than dilation. Only along the friction sleeve volumetric expansion can be observed in combination with plastic shear strains.

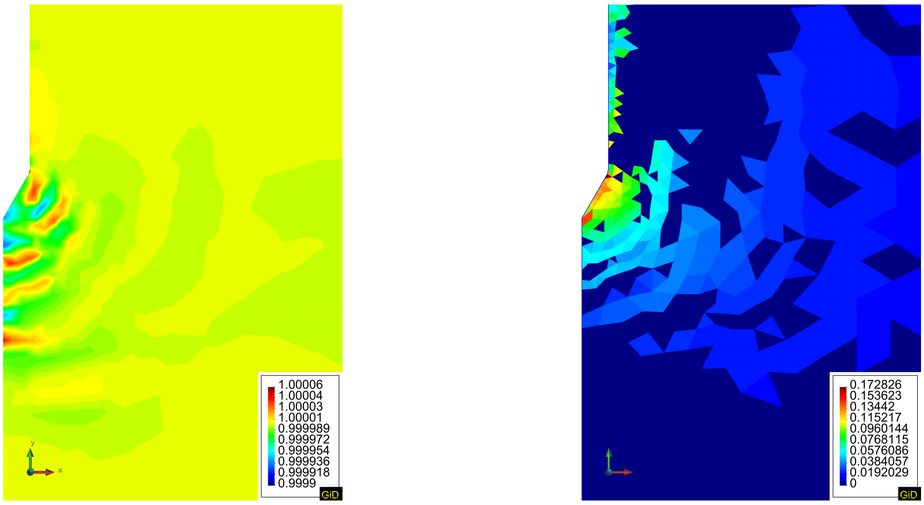

(a) (b)

Fig. 22 Contour plots of incremental Jacobian $\Delta\Theta$ (a) and incremental plastic shear strain (b) after 156 mm of penetration; $\Delta\Theta > 1$ equals volume expansion.

Eventually, the nodal Jacobian is evaluated in Fig. 23. The physical interpretation, whereupon increased volume change along the shaft of the penetrometer goes hand in hand with the advanced consolidation process at larger depth (see trend in Fig. 23 (a) to (c)), appears reasonable. Moreover, the fields look smooth suggesting adequate stabilization of the problem. Monitoring the behaviour of Θ gains in importance as the focus shifts more and more towards a drained situation. Throughout the computation Θ is repeatedly mapped from the nodes to the integration points and back in order to achieve smoothing and convergence of the calculation. For undrained conditions, Θ is close to 1 within the whole domain so the mapping has less influence. Now for larger changes of Θ the influence of the mapping parameters should be kept in mind for future computations.

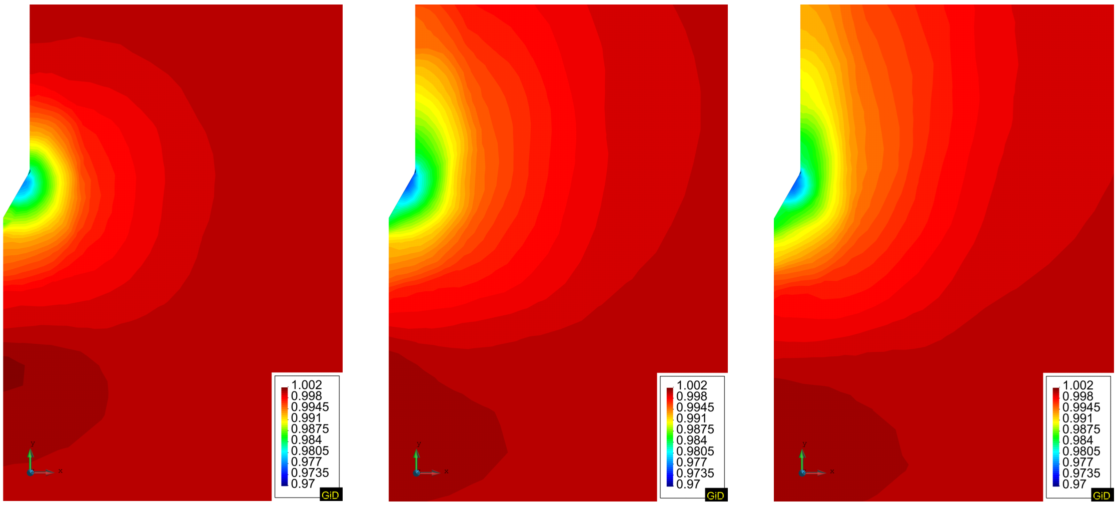

(a) (b) (c)

Fig. 23 Contour plots of nodal Jacobian Θ [-] around the cone after 56 mm (a), 156 mm (b) and 256 mm (c) of penetration; $\Theta > 1$ equals volume expansion.

5.3.2 Stress paths analysis

In addition to investigating the deformation behaviour of the soil, stress path analyses are carried out. Usually, a stress path is recorded for a fixed integration point. Due to the frequent remeshing, a fixed stress point position is defined. At each time step the closest integration point is searched and the stress invariants are stored. A grid of stress points was defined prior to the computation which is oriented along three vertical axes; along the symmetry axis, close to the cone shoulder (R = 0.0178 m) at a radial distance of 0.02 m and further away at 0.1 m from the symmetry axis. The stress points are situated at depths of up to 0.3 m below the starting position of the cone. The stress paths are illustrated in p-q diagrams in terms of both effective Kirchhoff or rather Cauchy stresses ($\boldsymbol{\tau}' = J\,\boldsymbol{\sigma}'$ and $\boldsymbol{\sigma}'$ respectively) and total Cauchy stresses $\boldsymbol{\sigma}$. Showing both $\boldsymbol{\sigma}'$ and $\boldsymbol{\tau}'$ helps to monitor the occurring volume change. The pore pressure at the integration point is obtained by interpolation using the element shape functions. However, caution with the interpretation of the resulting stress path is advised since firstly the resolution of the stress field based on a piecewise constant approximation is not very accurate and secondly the continuous change of integration points can lead to considerable jumps.

At first, the stress paths for the points P01 (0, -0.2) and P02 (0, -0.3) located on the centre axis below the cone are examined in Fig. 24 and Fig. 25: Initially, elastic unloading and reloading takes place until the yield surface is reached (0 – A). This goes hand in hand with a decrease and increase of the pore pressure. Then, undrained elasto-plastic loading takes place before eventually reaching the CS-line at point (B) while pore pressure is continuously built up with an increasing gradient. As expected for undrained behaviour, no differences between $\boldsymbol{\sigma}'$ and $\boldsymbol{\tau}'$ are evident so far. Subsequently, stress redistribution at CS occurs and the stress paths climb up the CS-line. Additional excess pore pressure builds up whereby the gradient starts to reduce (after passing B). Before the cone reaches the stress point the stress path for P01 (Fig. 24) exhibits short unloading behaviour due to increased isochoric loading. At this point $\boldsymbol{\sigma}'$ and $\boldsymbol{\tau}'$ start to differ slightly suggesting the onset of drainage and thus volumetric deformation. This is followed by deviatoric elasto-plastic loading and finally oscillations take over as CS is reached again at the final cone position.

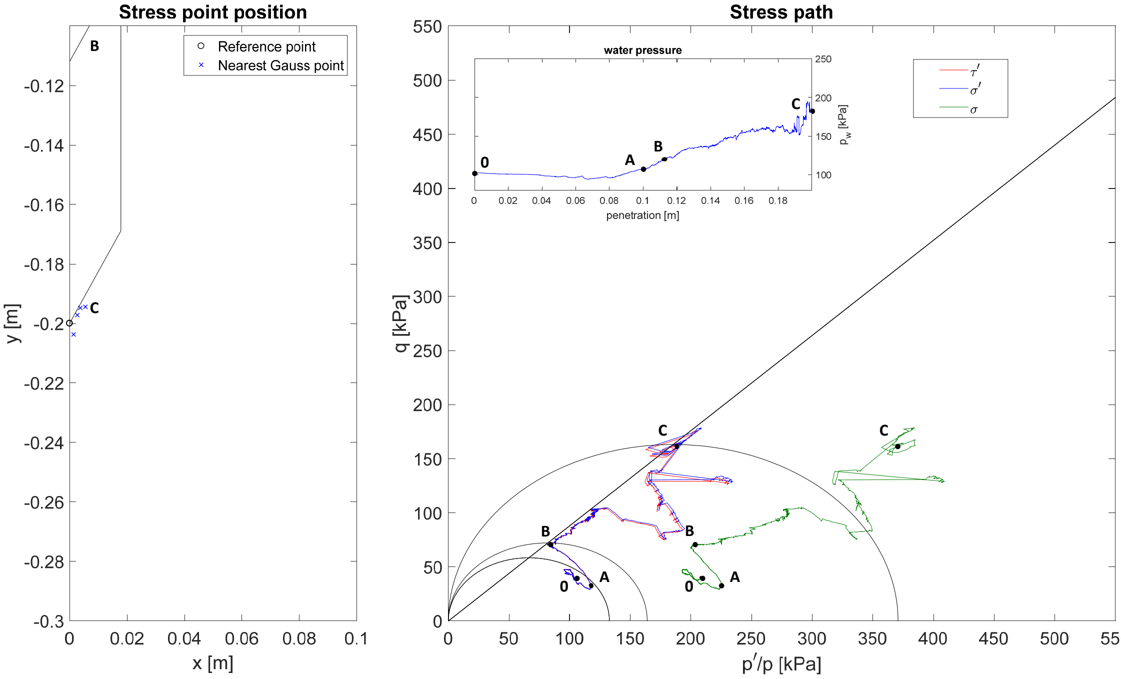

Fig. 24 Stress path for point P01 (0, -0.2): elastic unloading and loading (0 – A); undrained loading until CS (A – B); stress redistribution at CS and unloading before cone arrives at stress point (B – C).

Different behaviour is observed for the stress path at the deeper position P02 (Fig. 25). Similarly to P01, the stress paths climb up the CS-line after point B and the water pressure curve starts to flatten out. However, a sudden jump is observed due to a change of the stress point to the integration point of a neighbouring element. Fig. 26 shows the stress invariants P and J_2 at the penetration depth of 0.28 m where a spherical pattern of the stress state is evident below the cone. At this point, the closest integration point to the P02 position is about to jump from a stress state on the CS-line to a stress state with increased volumetric and reduced deviatoric stresses explaining the observed behaviour in the stress path.

The initial unloading in the stress path appears to explain the incremental volumetric

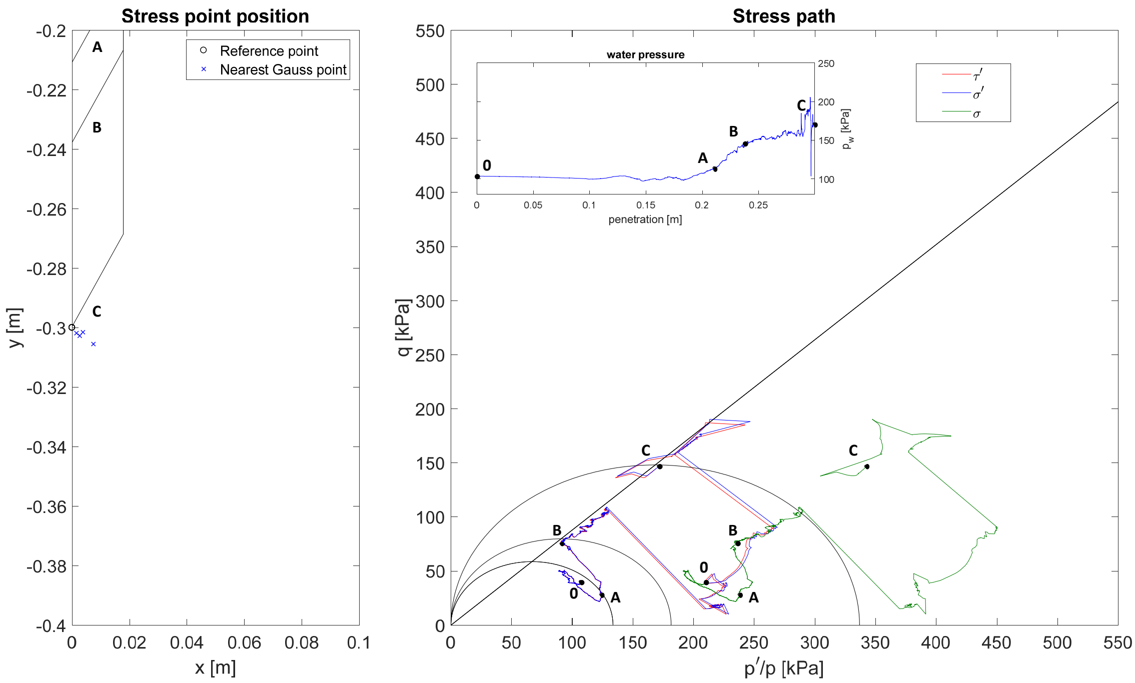

Fig. 25 Stress path for point P02 (0, -0.3): elastic unloading and loading (0 – A); undrained loading until CS (A – B); stress redistribution at CS with jump of stress point before cone arrives at stress point (B – C).

expansion and the resulting inward flow below the cone. Comparable behaviour is also found during pile installation. Sheng et al. (2005) showed in a numerical analysis of pile installation that volumetric expansion occurs at a distance of 3 to 5 times the pile diameter centrically below the tip which fits the observations made here qualitatively. Also, experiments by Dijkstra et al. (n.d.) on displacement piles confirm this deformation behaviour.

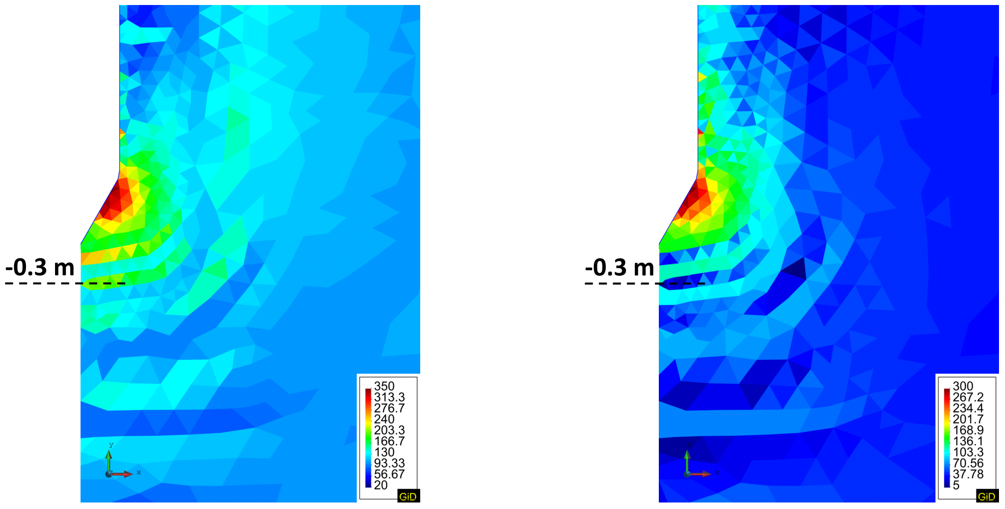

(a)

(b)

Fig. 26 Stress invariants P [kPa] (a) and J_2 [kPa] (b) at the penetration depth of 0.28 m.

An additional stress path for the point P19 (0.02, -0.2) at the side of the cone is shown in Fig. 27: Initially, elastic unloading is observed, however to a lesser extend compared to stress points P01 and P02. This makes sense since the expanding region is located centrically below the cone and thus the effect decreases with increasing radial distance from the centre axis. Then, undrained elasto-plastic loading takes place until reaching CS at point A. Again, a phase of stress redistribution follows and the stress path moves along the CS-line. The effective Kirchhoff and Cauchy stresses begin to show some differences. Again, a loop caused by increased volumetric loading followed by reaching the CS-line again is evident. Eventually, the stress path reaches point B as the shoulder of the cone has arrived and the water pressure reaches a maximum value of around 220 kPa after continuous built up. Both the stress paths and the water pressure start to oscillate. Subsequently, the cone moves on and unloading starts whereby section B to C, representing around 5 mm of penetration, is dominated by oscillations which makes the interpretation difficult. The pore pressure reduces significantly within this short period. Elastic unloading takes place afterwards until reaching the yield surface at point D while the pore pressure decreases more slowly. Finally, dilation takes place due to further unloading and the yield surface shrinks again. The computation stops at point D. It appears that the main effects of the cone passing by are captured within the time span of the computation and the future decay of pore pressure can be seen as a consolidation process. The observed dilation along the cone corresponds to the incremental volumetric expansion at the cone sleeve.

5.3.3 Summary

During the numerical study, the deformation behaviour of silts found by Paniagua et al. (2013) could not be reproduced with respect to the local drainage from compacting into expanding zones around the cone. Using the MCC model for normally consolidated soils results in noticeable dilation at the friction sleeve and local elastic unloading below a compacting region around the cone. However, the analysis of deformation and stress path behaviour helps to gain a better understanding on the process of CPT.

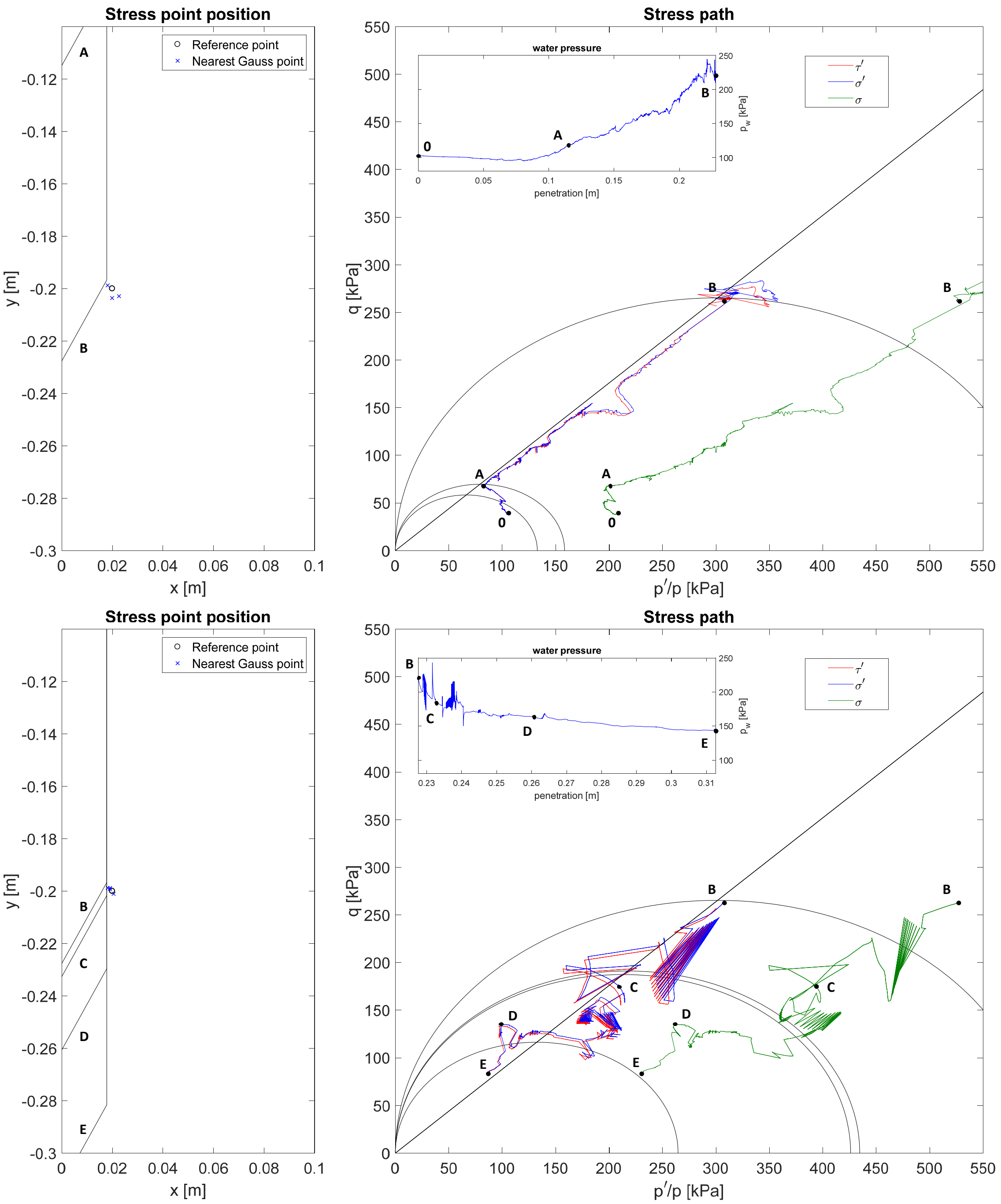

Fig. 27 Stress path for point P19 (0.02, -0.2): undrained loading until CS (0 – A); stress redistribution at CS (A – B); stress oscillation as cone shoulder passes by (B – C); elastic unloading (C – D); elasto-plastic unloading causing dilation (D – E).

6 Conclusion & Outlook

Thanks to the advanced G-PFEM application, numerical simulation of CPT appears to be a promising tool for the evaluation of CPT correlations. The fully coupled analysis allows to investigate partially drained conditions and gain better understanding of the soil-water interaction which has significant impact on the measured quantities.

In the present work, an 'on-the-fly' method for estimating the hydraulic conductivity based on the measured pore pressure was examined. Thereby, the semi-empirical approach requires partial drainage for the development of 'dynamic steady' flow and thus appears to be applicable for a first estimation of the permeability in silty soils. A more extended numerical study, by means of additional variation of soil permeability and mechanical soil properties, is expected to help defining the range of applicability.

The focus of the work was on the recalculation of an in-situ sounding which initially resulted in undrained system behaviour. Apart from the pore pressure, the measured and calculated tip resistance and sleeve friction showed a comparable order of magnitude between analysis and test. The effect of a rough compared to a smooth cone is neglectable for the assumed degree of friction between cone and soil. Further calculations with increased permeability led to reduced pore pressures and increased tip resistance fitting the in-situ measurement even better. Moreover, changing penetration velocities become evident under partially drained conditions.

Small scale experiments showed that local drainage takes place during CPT in silts as the water flows from compacting into expanding regions around the cone. This behaviour could not be entirely reproduced by means of numerical simulations. In fact, dilation was observable only along the shaft of the penetrometer. Local elastic unloading occurred below the compaction bulb at the cone tip, leading to volume increase and consequently local flow. The unloading below the penetrating body accords to observations during pile installations.

From the current point of view, future work involves more in-depth analysis of the numerical stabilization and mapping, with regard to changing drainage conditions. Other than that, the implementation of a constitutive law that accounts for the macroscopic structure of the material would be a reasonable next step.

7 Bibliography

Altenbach, H. (2015)
Kontinuumsmechanik. Berlin, Heidelberg: Springer Vieweg. 10.1007/978-3-662-47070-1

Bathe, K.-J. (2014)
Finite Element Procedures. Watertown: K.J. Bathe.

Borja, R.I.; Alarcón, E. (1995)
A mathematical framework for finite strain elastoplastic consolidation Part 1: Balance laws, variational formulation, and linearization. Computer Methods in Applied Mechanics and Engineering 122(1-2), 145-171.

Burns, S.E.; Mayne, P.W. (1998)
Monotonic and dilatory pore-pressure decay during piezocone tests in clay. Canadian Geotechnical Journal 35, 1063-1073.

Chai, J.C.; Agung, P.M.A.; Hino, T.; Igaya, Y.; Carter, J.P. (2011)
Estimating hydraulic conductivity from piezocone soundings. Géotechnique 61(8), 699-708.

Chen, G.J. (2004)
Consolidation of multilayered half space with anisotropic permeability and compressible constituents. International Journal of Solids and Structures, 41, 4567-4586.

Coussy, O. (2004)
Poromechanics. Chichester: Wiley. 10.1002/0470092718

Dadvand, P.; Rossi, R.; Oñate, E. (2010)
An Object-oriented Environment for Developing Finite Element Codes for Multi-disciplinary Applications. Arch Comput Methods Eng 17, 253-297.

Dijkstra, J.; Broere, W.; Frits van Tol, A. (n.d.)
Experimental investigation into the stress and strain development around a displacement pile.

Elsworth, D.; Lee, D.S. (2005)
Permeability Determination from On-the-Fly Piezocone Sounding. Journal of Geotechnical Geoenvironmental Engineering 131(5), 643-653.

Elsworth, D.; Lee, D.S. (2007)
Limits in determining permeability from on-the-fly uCPT sounding. Géotechnique 57(8), 679-685.

Felippa, C.A. (2004)
Introduction to Finite Element Methods [lecture notes]. Department of Aerospace Engineering Sciences and Center for Aerospace Structures. Univerity of Colorado at Boulder.

Kelly, P. (2012)
Foundations of Continuum Mechanics [lecture notes]. Faculty of Engineering. University of Auckland.

Larsson, J.; Larsson, R. (2002)
Non-linear analysis of nearly saturated porous media: theoretical and numerical formulation. Comput. Methods Appl. Mech. Engrg. 191, 3885-3907.

Lunne, T.; Robertson, P.K.; Powell, J.J.M. (1997)
Cone penetration testing in geotechnical practice. New York: Blackie Academic/Routledge Publishing.

Monforte, L.; Carbonell, J.M.; Arroyo, M.; Gens, A. (2016)
Performance of mixed formulations for the particle finite element method in soil mechanics problems. Computational Particle Mechanics, 1-16.

Monforte, L.; Arroyo, M.; Carbonell, J.M.; Gens, A. (2017)
Numerical simulation of undrained insertion problems in geotechnical engineering with the Particle Finite Element Method (PFEM). Computers and Geotechnics 82, 144-156.

Oñate, E.; Idelsohn, S.R.; Celigueta, M.A.; Rossi, R.; Marti, J.; Carbonell, J.M.; Ryzakov, P.; Suárez, B. (2011)
Advances in the particle finite element method (PFEM) for solving coupled problems in engineering. Particle-Based Methods, 1-49.

Paniagua, P.; Andò, E.; Silva, M.; Emdal, A.; Nordal, S.; Viggiani, G. (2013)
Soil deformation around a penetrating cone in silt. Géotechnique Letters 3, 185-191.

Preisig, M.; Prévost, J. H. (2011)
Stabilization procedures in coupled poromechanics problems: A critical assessment. Int. J. Numer. Anal. Meth. Geomech. 35, 1207-1225.

Sachsenhofer, M. (2012)
Comparison of correlations from CPTu, SPT, DP. Master's Thesis. Technische Universität Graz.

Sheng, D.; Eigenbrod, K.D.; Wriggers, P. (2005)
Finite element analysis of pile installation using large-slip frictional contact. Computers and Geotechnics 32, 17-26.

Sun, W.; Ostien, J.T.; Salinger, A.G. (2013)
A stabilized assumed deformation gradient finite element formulation for strongly coupled poromechanical simulations at finite strain. Int. J. Numer. Anal. Meth. Geomech. °37, 2755-2788.